Multimodel simulations of carbon monoxide: Comparison with observations and projected near-future changes

D. T. Shindell, G. Faluvegi, D. S. Stevenson, M. C. Krol, 4.4 L. K. Emmons, 5 J.-F. Lamarque, ⁵ G. Pétron, ⁶ F. J. Dentener, ⁷ K. Ellingsen, ⁸ M. G. Schultz, ^{9,10} O. Wild, ^{11,12} M. Amann, ¹³ C. S. Atherton, ¹⁴ D. J. Bergmann, ¹⁴ I. Bey, ¹⁵ T. Butler, ¹⁶ J. Cofala, ^{9,13} W. J. Collins, ¹⁷ R. G. Derwent, ¹⁸ R. M. Doherty, ² J. Drevet, ¹⁵ H. J. Eskes, ¹⁹ A. M. Fiore, ²⁰ M. Gauss, ⁸ D. A. Hauglustaine, ²¹ L. W. Horowitz, ²⁰ I. S. A. Isaksen, ⁸ M. G. Lawrence, ¹⁶ V. Montanaro,²² J.-F. Müller,²³ G. Pitari,²² M. J. Prather,²⁴ J. A. Pyle,²⁵ S. Rast,⁹ J. M. Rodriguez, ²⁶ M. G. Sanderson, ¹⁶ N. H. Savage, ²⁵ S. E. Strahan, ²⁶ K. Sudo, ¹¹ S. Szopa, ²¹ N. Unger, ¹ T. P. C. van Noije, ¹⁹ and G. Zeng²⁵

Received 20 January 2006; revised 15 June 2006; accepted 30 June 2006; published 14 October 2006.

[1] We analyze present-day and future carbon monoxide (CO) simulations in 26 state-ofthe-art atmospheric chemistry models run to study future air quality and climate change. In comparison with near-global satellite observations from the MOPITT instrument and local surface measurements, the models show large underestimates of Northern Hemisphere (NH) extratropical CO, while typically performing reasonably well elsewhere. The results suggest that year-round emissions, probably from fossil fuel burning in east Asia and seasonal biomass burning emissions in south-central Africa, are greatly underestimated in current inventories such as IIASA and EDGAR3.2. Variability among models is large, likely resulting primarily from intermodel differences in representations and emissions of nonmethane volatile organic compounds (NMVOCs) and in hydrologic cycles, which affect OH and soluble hydrocarbon intermediates. Global mean projections of the 2030 CO response to emissions changes are quite robust. Global mean midtropospheric (500 hPa) CO increases by 12.6 ± 3.5 ppby (16%) for the high-emissions (A2) scenario, by 1.7 ± 1.8 ppbv (2%) for the midrange (CLE) scenario, and decreases by 8.1 ± 2.3 ppbv (11%) for the low-emissions (MFR) scenario. Projected 2030 climate changes decrease global 500 hPa CO by 1.4 ± 1.4 ppbv. Local changes can be much larger. In response to climate change, substantial effects are seen in the tropics, but intermodel variability is quite large. The regional CO responses to emissions changes are robust across models, however. These range from decreases of 10-20 ppbv over much of the industrialized NH for the CLE scenario to CO increases worldwide and year-round under A2, with the

Copyright 2006 by the American Geophysical Union. 0148-0227/06/2006JD007100

D19306 1 of 24

¹NASA Goddard Institute for Space Studies, Columbia University, New York, New York, USA.

School of Geosciences, University of Edinburgh, Edinburgh, UK.

³Space Research Organisation Netherlands, Utrecht, Netherlands.

⁴Also at Wageningen University and Research Centre, Wageningen, Netherlands.

⁵Atmospheric Chemistry Division, National Center for Atmospheric Research, Boulder, Colorado, USA.

Global Monitoring Division, Earth System Research Laboratory, NOAA, Boulder, Colorado, USA.

Joint Research Centre, Institute for Environment and Sustainability,

European Commission, Ispra, Italy.

⁸Department of Geosciences, University of Oslo, Oslo, Norway.

⁹Max Planck Institute for Meteorology, Hamburg, Germany.

¹⁰Now at Institute for Chemistry and Dynamics of the Geosphere: Troposphere, Research Center Jülich, Jülich, Germany.

Frontier Research Center for Global Change, Japan Agency for Marine-Earth Science and Technology, Yokohama, Japan.

¹²Now at Centre for Atmospheric Science, University of Cambridge, Cambridge, UK.

¹³International Institute for Applied Systems Analysis, Laxenburg, Austria.

¹⁴Atmospheric Science Division, Lawrence Livermore National Laboratory, Livermore, California, USA.

¹⁵Ecole Polytechnique Fédéral de Lausanne, Lausanne, Switzerland.

¹⁶Max Planck Institute for Chemistry, Mainz, Germany.

¹⁷Met Office, Exeter, UK.

¹⁸rdscientific, Newbury, UK.

¹⁹Atmospheric Composition Research, Royal Netherlands Meteorological Institute, De Bilt, Netherlands.

²⁰Geophysical Fluid Dynamics Laboratory, NOAA, Princeton, New

Jersey, USA.

²¹Laboratoire des Sciences du Climat et de l'Environnement, Gif-sur-

Yvette, France.

²Dipartimento di Fisica, Università L'Aguila, L'Aguila, Italy.

²³Belgian Institute for Space Aeronomy, Brussels, Belgium.

²⁴Department of Earth System Science, University of California, Irvine, California, USA.

²⁵Centre for Atmospheric Science, University of Cambridge, Cambridge, UK.

⁶Goddard Earth Science and Technology Center, Greenbelt, Maryland,

largest changes over central Africa (20-30 ppbv), southern Brazil (20-35 ppbv) and south and east Asia (30-70 ppbv). The trajectory of future emissions thus has the potential to profoundly affect air quality over most of the world's populated areas.

Citation: Shindell, D. T., et al. (2006), Multimodel simulations of carbon monoxide: Comparison with observations and projected near-future changes, *J. Geophys. Res.*, 111, D19306, doi:10.1029/2006JD007100.

1. Introduction

- [2] Carbon monoxide is a precursor to tropospheric ozone (O₃), it influences the abundance of OH and hence the tropospheric oxidation capacity and methane, and it is a source of carbon dioxide (CO₂). It thus affects the three most important greenhouse gases contributing to the radiative forcing increases since the preindustrial era. It also plays an important role in air quality by affecting O₃ and the lifetime of a host of reduced species via OH. Of all the tropospheric primary pollutants, CO is among the best observed in the troposphere on the global scale from satellites. It is the only pollutant for which global satellite data includes measurements of the vertical profile, albeit with limited resolution. Observations of CO from the surface and from aircraft are also available and in the case of the surface data, cover a much longer period than the satellite records. Thus in addition to being important for understanding both air quality and climate, CO is in many ways an ideal species to use in evaluation of global models. This is particularly true because of its relatively long lifetime in the troposphere (\sim 1 month). This means that CO provides an integrated view of regional emissions and transport that short-lived species do not, and that it is less sensitive to intermodel differences in resolution, emission height, etc. than are shorter-lived species.
- [3] Tropospheric CO is directly emitted at the Earth's surface and is also produced chemically by the oxidation of hydrocarbons in the troposphere. Both direct and indirect sources include a mixture of contributions from natural and anthropogenic activities. A large number of models have been used to simulate CO previously [Kanakidou et al., 1999; Prather et al., 2001]. These simulations were evaluated using the sparse surface and aircraft data available at the time, which generally did not allow identification of regional biases.
- [4] Ice cores suggest that the abundance of CO in the atmosphere gradually decreased over the last two millennia prior to the industrial revolution, perhaps indicative of a reduction in biomass burning emissions [Ferretti et al., 2005]. Historical emissions inventories indicate that anthropogenic sources of both CO and hydrocarbons (as well as other ozone precursors) have grown dramatically during the last 100 years [van Aardenne et al., 2001]. It is unclear how global CO emissions will evolve in the future and various scenarios predict either a renewed decrease or a continued increase depending mostly on the development in Asia. To explore the response of CO to these changes, as well as to climate change, a large suite of state-of-the-art chemical models were run using similar present-day and future boundary conditions, in part to make results available for the forthcoming Intergovernmental Panel on Climate Change (IPCC) Fourth Assessment Report (AR4) [Dentener et al., 2005a; Stevenson et al., 2006]. We report here on a comparison of the CO simulations between those models

and observations, and on the projected changes in the models between the present-day and 2030.

2. Model Simulations, Observations, and Comparative Analysis Methodology

2.1. Models

- [5] We analyze simulations of CO from twenty-six three-dimensional global models (Table 1). Nearly all models were run in a Chemistry-Transport Model (CTM) configuration, for which changes in chemical constituents do not affect the radiation and hence meteorology, even for those models running chemistry within General Circulation Models (GCMs). In some cases, the same CTM was driven by more than one set of meteorological fields derived either from weather prediction analyses or from GCMs. Most used fields for the year 2000. Climate change simulations were performed by ten of the models (Table 1). The CTMs generally performed simulations for just one year for each scenario, while the chemistry-GCMs typically simulated 5 to 10 years for each set of boundary conditions.
- [6] While the models all aim to simulate tropospheric chemistry and thus include many of the same constituents, chemical reactions and physical processes, there are nevertheless substantial differences among models. The complexity of the chemical schemes, especially the portion concerned with hydrocarbon oxidation, varies greatly from model to model. Some models include heterogeneous interactions between chemistry and aerosols, while others do not. On the physical side, chemistry is closely coupled with the hydrologic cycle via transport, e.g., in convective plumes, and via removal of soluble gases, so that large intermodel differences in representation of cloud processes and hydrologic processes in general will influence chemistry. The models also use a variety of resolutions, with the horizontal ranging from $10^{\circ} \times 22.5^{\circ}$ to $1.9^{\circ} \times 1.9^{\circ}$ (and in one model, $1^{\circ} \times 1^{\circ}$ in some areas), and the vertical from 9 to 52 levels. The vertical structure varies in layer thicknesses as a function of altitude and in the location of the model top as well as in the number of layers. The models have rather different treatments of the transport of ozone from the stratosphere to the troposphere as well, which affects their simulations of tropospheric ozone and hence OH and CO. Finally, the models use a variety of methods to calculate photolysis rates. A more in-depth discussion of the models is given in [Stevenson et al., 2006], but the reader is referred to the publications by the participating groups for complete information on the models, which are summarized in Table A1 in Appendix A.

2.2. Simulations

[7] The experiments consisted of a control simulation, three projections of future emissions, and one simulation with both projected future emissions and climate (Table 2). The three projected emissions changes (S2/CLE, S3/MFR,

Table 1. Global Ozone, OH, and CO in the Models^a

	Climate				OH Weighted	
	Change		Inverse OH	Global Mean OH,	by k _{CO+OH} ,	Global Mean Annual
	Run	B _{O3} , Tg	(as τ_{CH4} Chemical, yr)	10 ⁵ molec cm ⁻³	10 ⁵ molec cm ⁻³	Average CO, ppbv
CHASER CTM	no	331	9.53	11.1	11.3	79.6
CHASER GCM	yes	333	9.46	11.4	11.6	79.6
FRSGC UCI	no	331	8.50	11.8	12.0	79.4
GEOS-CHEM	no	294	11.83	9.4	9.5	91.6
GISS	yes	341	9.61	11.5	11.5	68.3
MOZ2-GFDL	no	349	9.53	10.9	11.2	83.1
GMI/CCM	no	388	8.37	14.3	14.2	66.4
GMI/DAO	no	386	8.54	13.2	13.2	71.2
GMI/GISS	no	372	9.68	12.9	12.9	69.4
IASB	no	377	9.15	11.8	12.0	76.1
LLNL-IMPACT	no	406	7.97	13.5	13.7	64.9
LMDz/INCA (CTM)	no	330	9.72	11.0	11.1	77.0
LMDz/INCA (GCM)	yes	316	9.99	10.7	10.8	78.1
MATCH-MPIC-NCEP	no	399	10.91	9.6	9.8	85.8
MATCH-MPIC-ECMWF	no	377	nr	9.8	10.0	83.9
MOZECH	yes	407	6.91	13.7	13.9	70.2
MOZECH2	yes	387	7.95	nr	nr	75.8
MOZART4-NCAR	yes	375	10.37	10.6	10.7	83.8
OsloCTM2	no	nr	8.00	9.1	9.2	71.1
p-TOMCAT	no	248	15.05	7.1	7.3	91.9
STOCHEM-HadAM3	yes	274	9.55	11.6	11.8	81.5
STOCHEM-HadGEM	yes	293	12.09	9.2	9.4	92.6
TM4	no	344	10.02	10.4	10.5	80.6
TM5	no	339	8.91	11.9	12.0	66.5
ULAQ	yes	328	9.07	13.0	13.2	57.6
UM CAM	yes	303	12.38	8.9	9.0	88.6
Multimodel mean	no	345	9.72	11.1	11.3	77.5
Standard deviation, % of mean	no	42 (12%)	1.7 (17%)	1.7 (15%)	1.7 (15%)	9.2 (12%)
Spread, % of mean	no	159 (46%)	8.1 (84%)	7.2 (65%)	6.9 (61%)	35 (45%)
Observations	no		9.6 ± 1.4			87.2 ± 3.2

^aGlobal mean CO is reported for the broad MOPITT 500 hPa retrieval level for all models. Tropospheric ozone burdens ($\mathbf{B_{O3}}$) are taken from *Stevenson et al.* [2006]. The observed methane lifetime is based on indirect constraints primarily from methyl chloroform observations [*Prather et al.*, 2001], while the observed CO is from the MOPITT 2000–2004 data. OH is the global mean mass-weighted value below the nominal tropopause following the surface defined by $300-215 \times \cos(\text{lat})^2$ hPa (and using the temperature and pressure grid of the TM model to transform from mixing ratio to density when required). OH weighted by the local rate coefficient of the CO+OH reaction is also shown; nr means not reported.

and S4/A2) used the same meteorology and climate as the control (S1), so the difference between these reflects only the influence of altered emissions. Simulation S5 included both projected future emissions and climate, with the climate changes coming from the individual underlying GCMs in the ten participating models (Table 1). The climate changes were based upon a variety of emissions projections, including the A2, B1 and IS92a scenarios, providing a range of climate changes (though differences between the scenarios are still small at 2030, becoming more important later in the 21st century). This simulation can then be compared with the control (S1) to see the effects of both changes, or compared with the simulation with the same emissions projections but not climate change (S2) to isolate the impact of the climate.

[8] Emissions of CO and NMVOCs were based on the IIASA (International Institute for Applied Systems Analysis) data set of [Dentener et al., 2005b], which scaled EDGAR3.2 1995 emissions using national/sector development to derive 2000 emissions and included the biomass burning inventory of [Van der Werf et al., 2003] averaged over 1997–2002. Injection heights for emissions from burning were supplied, however many models did not use this information. Direct CO emissions for the present-day were 470 Tg(CO)/yr from entirely anthropogenic sources (fuel combustion and industry), 507 Tg(CO)/yr from biomass burning, and 100 Tg(CO)/yr from oceans and vegetation (Table 3). The latter two were unchanged across all scenarios for CO, and similarly burning emissions were unchanged for all species across all scenarios. The anthro-

Table 2. Simulations Performed

Name	Description	Meteorology	Emissions	Reference
S1	control (2000)	1995-2004	2000 IIASA, EDGAR3.2 distribution	Dentener et al. [2005b], Olivier and Berdowski [2001]
S2'	current legislation (CLE)	1995-2004	2030 IIASA CLE	Dentener et al. [2005b]
S3	maximum feasible reduction (MFR)	1995-2004	2030 IIASA MFR	Dentener et al. [2005b]
S4	IPCC A2	1995-2004	2030 SRES A2	Nakicenovic et al. [2000]
S5	current legislation plus climate change	2025-2034	2030 IIASA CLE	Stevenson et al. [2005]

Table 3. Emissions of CO, NMVOCs, and NO_x and CH₄ Mixing Ratios for Each Scenario^a

	Natural Emissions (All Runs)	Biomass Burning (All Runs)	Anthro S1	Anthro S2	Anthro S3	Anthro S4	Anthro S5
CO, Tg/yr	100	507	470	397	222	761	397
NMVOCs, Tg C/yr	512 (isoprene), 260 (terpenes)	31	116	114	73	176	114
NO _x , Tg N/yr	12	10.2	27.8	32.8	13.1	54.6	32.8
CH ₄ , ppbv		• • •	1760	2088	1760	2163	2012

 a Anthro indicates anthropogenic emissions. Scenarios are as in Table 2. NMVOC emissions are recommended values. Some models did not include all NMVOC species, and some calculated isoprene emissions internally. Natural emissions of NO_x include 5 Tg/yr from lightning and 7 Tg/yr from soils, a value that includes some contribution from anthropogenic fertilizer application. In practice, many of the models calculate lightning NO_x emissions on the basis of their internal convection schemes, and thus a range of 3.7-7.0 Tg/yr was used.

pogenic source of CO did vary for each scenario, however, as did anthropogenic emissions of NMVOCs and NO_x (Table 3). Methane mixing ratios for future conditions were prescribed in the models using results from prior simulations with the STOCHEM_HadAM3 model [Dentener et al., 2005b; Stevenson et al., 2005]. Anthropogenic emissions of SO₂ and NH₃ also varied according to the scenario projections [Stevenson et al., 2006].

[9] Though the CO emission scenarios used were the same for all models, emissions of NMVOCs varied. Total NMVOC emissions from anthropogenic and biomass burning were prescribed, and it was recommended that models apportion these following the IPCC Third Assessment Report (TAR [Prather et al., 2001, Table 4.7]). This allowed individual species' emissions to be derived and groups of chemically related NMVOC compounds to be formed that fit the particular model's chemistry schemes. However, as these schemes differ widely and the NMVOC grouping is not always straightforward, models ended up using varying fractions of the total NMVOC emissions and the reactivity and reaction products of the emitted NMVOC also differ. Biogenic emissions were even more varied among the models, with many calculating emissions of gases such as isoprene interactively on the basis of their model climates. This led to a range of emissions of 220-631 Tg C/yr for isoprene emissions, though 24 of the 26 models had emissions in the range of 380-550 Tg C/yr. Biogenic emissions of other species, such as terpenes, varied at least as widely, as many models did not include these at all.

[10] The direct CO emissions used here, 1077 Tg(CO)/yr, are substantially less than the 1550 Tg(CO)/yr used in the TAR. The difference is largely driven by changes in biomass burning emission inventories, for which recent studies [Van der Werf et al., 2003] (upon which the sources used here are based) show substantially smaller values than earlier studies [Bergamaschi et al., 2000].

2.3. Observations

[11] The present-day model simulations can be evaluated by comparison with observations. We concentrate here on global satellite measurements of CO from the MOPITT instrument as the most suitable for comparison with global models. We use data from April 2000 through April 2001 and from September 2001 to December 2004 [*Emmons et al.*, 2004]. In between these times, a cooler failure caused a break in the record. MOPITT data is reported as retrievals at seven vertical levels. The sensitivity of the retrievals to the true atmospheric profile is described by averaging kernels, which also incorporate a priori information [*Deeter et al.*,

2003]. The averaging kernels (A) indicate the relative weighting between the a priori (x_a) and true CO profiles (x):

$$\mathbf{x}_{\text{MOP}} = \mathbf{A}\mathbf{x} + (\mathbf{I} - \mathbf{A})\mathbf{x}_{\mathbf{a}} \tag{1}$$

where I is the identity matrix.

- [12] The MOPITT averaging kernels depend upon surface emissivity and temperature, and therefore vary in space and time. Proper comparison with a model thus requires that the model profiles be transformed according to equation (1) using the space- and time-varying averaging kernels from the MOPITT retrievals.
- [13] Although seven retrieval levels are reported, the MOPITT profiles typically have only 1 to 2 independent points (degrees of freedom) [Deeter et al., 2004]. We thus concentrate on the 500 hPa retrieval level, a broad retrieval that effectively samples much of the middle troposphere. The 350 and 850 hPa levels are also used, but only to capture the independent upper and lower-tropospheric data (where available) by contrasting these regions with one another. Thus, although the instrument's sensitivity is very low near the surface, so that the 850 level represents a broad area of the lower troposphere often peaking above 850 hPa, it should nevertheless provide a contrast with the upper tropospheric levels over much of the globe.
- [14] We use monthly mean daytime values derived from version 3 retrievals. These data are gridded at a resolution of 1 by 1 degree, and the models' coarser grids are subsampled at this same resolution for comparison. The version 3 retrievals use a uniform worldwide a priori CO profile based on observations. As the observations are largely from the polluted NH, the profile tends to be too large in the Southern Hemisphere (SH) and leads to a systematic positive bias there. Comparisons between the model and MOPITT will not be affected by this bias, however, as the a priori information cancels out of differences since the model is sampled like MOPITT observations (equation (1)). Biases may also be induced by the differences between the models' full temporal and spatial averaging and the satellite's limited sampling time and exclusion of cloudy areas, but given the relatively long lifetime of CO these are expected to be quite small. On the basis of a detailed evaluation against aircraft observations, mean biases in MOPITT range from about 7% in the lower troposphere to 3% in the upper troposphere, with the largest biases occurring over clean locations [Emmons et al., 2004].
- [15] Comparisons are also made between the annual cycle of surface CO in the models and measurements from the NOAA Global Monitoring Division (GMD, formerly

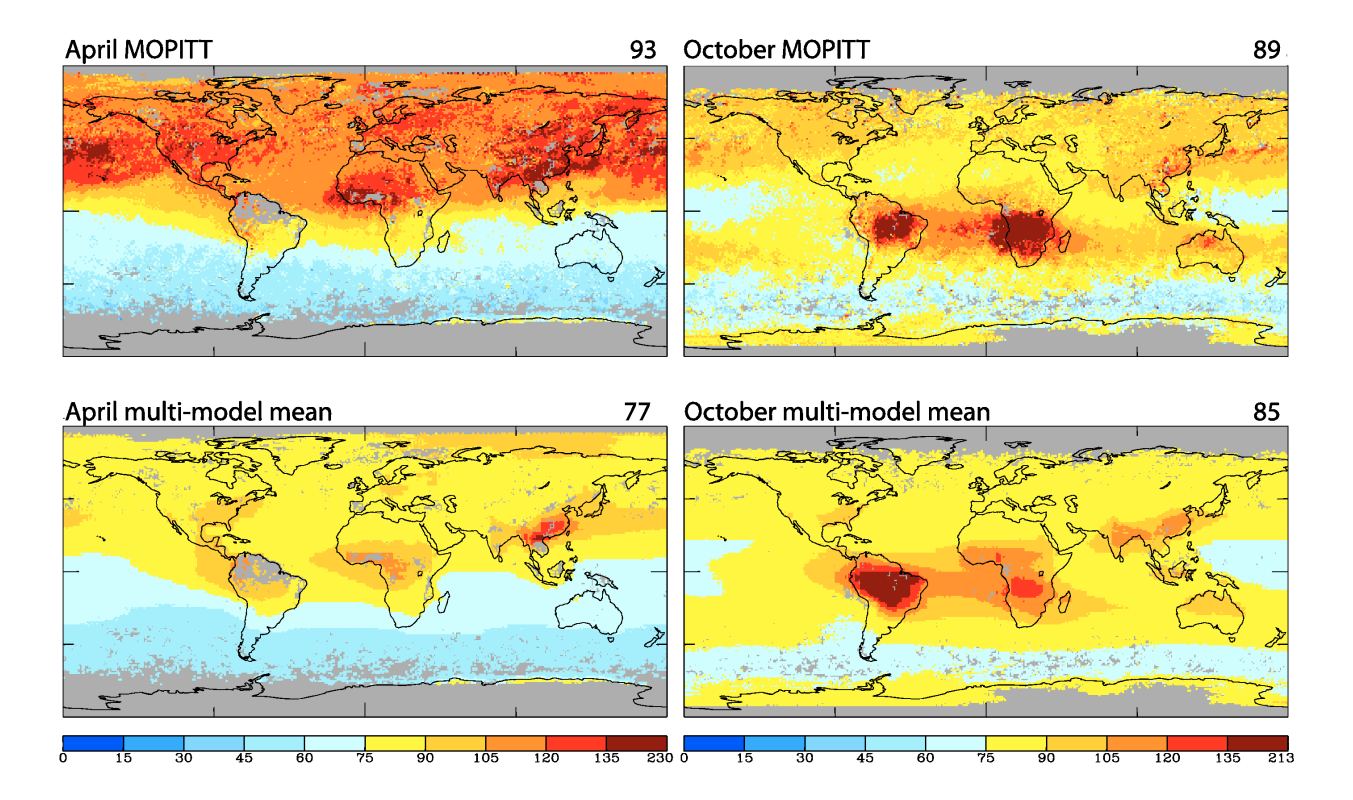


Figure 1. MOPITT and multimodel CO (ppbv). (top) MOPITT observations from 2000 for April (left) and October (right) for the 500 hPa retrieval level. (bottom) Equivalent fields for the multimodel ensemble average when all the S1 simulations are sampled with the MOPITT averaging kernel and a priori CO profiles. Values in the top right corner are the global mean area-weighted CO (ppbv). Grey areas indicate no data.

CMDL) network [Novelli et al., 1998]. These observations have been made at generally remote sites that can be difficult for relatively coarse resolution global models to reproduce, but are long term and extremely reliable. We use these observations averaged over all available 1990s monthly mean data (6–10 years), and also show comparisons with the year 2000 alone as many of the CTMs simulated this year specifically.

2.4. Analyses

[16] Model simulations are averaged over all available years of output to produce monthly mean fields. For the comparison of present-day results with MOPITT data, model CO fields have been transformed with the MOPITT monthly mean averaging kernels and the MOPITT retrieval CO a priori profile (equation (1)) from April 2000 through March 2001. The influence of changes in the averaging kernels from year to year on the 500 hPa retrievals has been shown to be quite small, typically 2 ppbv or less for continental scales [Shindell et al., 2005a] and presumably smaller for the larger regions used here, so we have not adjusted the MOPITT values from other years to match the 2000–2001 sampling as would be required for a strict quantitative model/data comparison. All mean values discussed here are calculated using area-weighting.

[17] Both analyses of atmospheric observations and bottomup estimates of CO sources have indicated substantially increased CO emissions from boreal burning, primarily in Russia, associated with elevated CO during 2002–2003 [Edwards et al., 2004; Kasischke et al., 2005; Yurganov et al., 2005]. As the emissions inventory used in this study does not include such extensive boreal burning, we compare the model results with MOPITT measurements averaged over 2000, 2001 and 2004 as well as the entire 5 year period.

[18] For comparison with the GMD surface data we use the models' lowest layer values at all sites except for the high-elevation sites of Mauna Loa and Niwot Ridge, where we used the first layer with pressure below 680 hPa to examine a comparable altitude. The lowest layer depth ranged from about 35 m to 800 m in the models, which will influence the comparison with the observations, especially for those with thicker lowest layers (though model values are influenced by other factors such as the treatment of turbulent mixing in the boundary layer and emission injection height as well).

3. Present-Day Results

[19] Models are able to capture many aspects of the global spatial distribution of CO as observed by MOPITT, which we examine here focusing on the springtime CO maximum in the NH (April) and the SH biomass burning season (October). The models successfully reproduce the maxima over South America and southern Africa during the austral biomass burning season and the low values seen

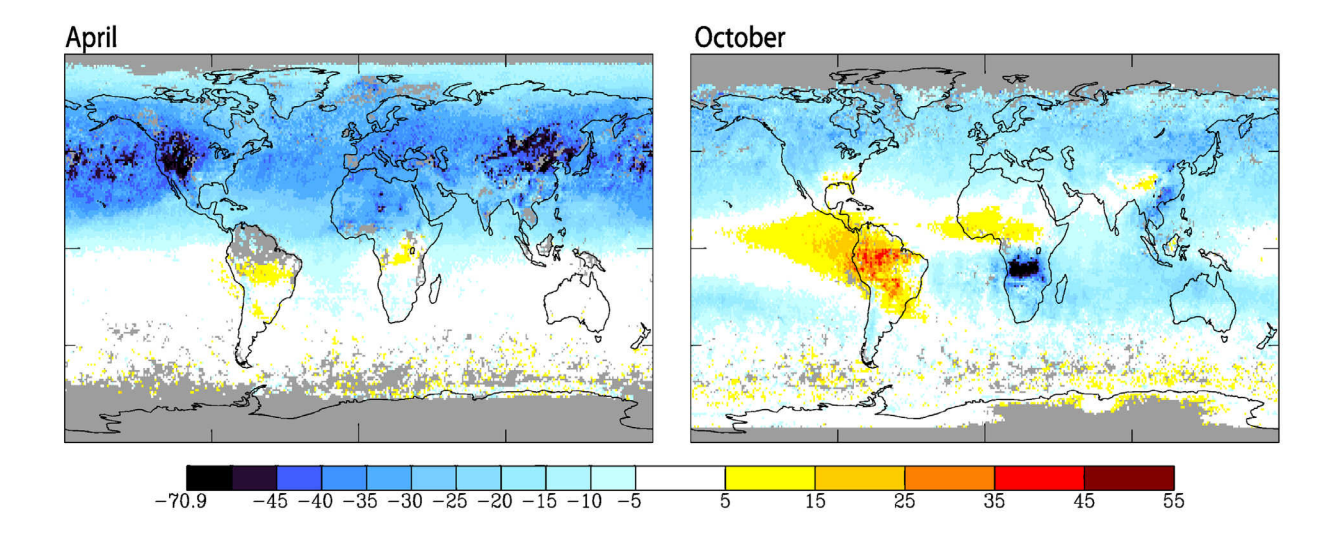


Figure 2. Differences between MOPITT 2000–2004 averages and multimodel average CO (ppbv). Values are shown for (left) April and (right) October for the 500 hPa retrieval level.

over tropical and SH oceans (Figure 1). In the NH, however, the average model strongly underestimates the abundance of CO over both land areas and ocean regions. The discrepancies are especially large during boreal spring, as seen in the difference between the multimodel average and the MOPITT observations (Figure 2). Underpredictions of more than 60 ppbv occur in the lower troposphere over east Asia, with biases in excess of 40 ppbv over much of North America, Europe and the North Pacific during April. During the SH biomass burning season (austral spring), midtropospheric CO is much better simulated over nearly the entire globe, though northern extratropical values are still generally too low and especially large underestimates persist over east Asia. CO over continental areas in the SH and in the tropics also shows substantial differences with respect to observations. There are slight underestimates over Australia and large underestimates over south-central Africa, where they again exceed 60 ppbv. Slight overestimates are seen over equatorial and western Africa with larger positive biases (>40 ppbv) over tropical South America, extending out over the tropical eastern Pacific following the trade winds. These biases lead to substantially reduced spatial correlations between MOPITT observations and the models during October in comparison with April (Table 4). The boreal springtime correlations are in fact quite high despite the underestimate of CO in the NH extratropics, indicating that the models have captured the spatial structure of the CO distribution relatively well. The spatial correlations are quite sensitive to emissions however, so must be interpreted with caution. For example, simulations using different emissions inventories with the identical GISS model found 850 hPa correlations during April that were 0.14 higher and during October that were 0.28 higher [Shindell et al., 2005a].

[20] Examining the annual cycle of global mean CO (Figure 3, top left) reveals that systematic underestimates of CO persist throughout the year for the multimodel average, with the largest underestimates occurring during boreal spring. Looking at the models individually (Figure 3, top right), most models fail to reproduce the increase in

global mean CO from boreal winter to spring seen in observations, even some of those with large springtime values. Additionally, the NH July minimum and SH October maximum are often a month early in the models. The models span a broad range of values with a fairly continuous distribution (aside from the ULAQ model, which is

Table 4. Correlation Coefficients Between Model and MOPITT Global Retrievals^a

Model	April 850 hPa	April 350 hPa	October 850 hPa	October 350 hPa
CHASER-CTM	0.90	0.87	0.54	0.61
CHASER-GCM	0.89	0.89	0.47	0.57
FRSGC-UCI	0.87	0.78	0.70	0.73
GEOS-CHEM	0.90	0.91	0.60	0.62
GISS	0.80	0.92	0.52	0.75
GMI-CCM	0.85	0.73	0.70	0.60
GMI-DAO	0.87	0.85	0.70	0.65
GMI-GISS	0.71	0.70	0.66	0.64
IASB	0.78	0.75	0.41	0.50
LLNL-IMPACT	0.86	0.91	0.56	0.59
LMDZ/INCA-CTM	0.84	0.79	0.54	0.63
LMDZ/INCA-GCM	0.88	0.88	0.45	0.52
MATCH-MPIC-ECMWF	0.90	0.86	0.53	0.60
MATCH-MPIC-NCEP	0.90	0.90	0.43	0.53
MOZART2-GFDL	0.86	0.79	0.59	0.60
MOZART4-NCAR	0.89	0.84	0.59	0.60
MOZECH	0.80	0.80	0.59	0.66
MOZECH2	0.80	0.76	0.58	0.65
OsloCTM2	0.89	0.92	0.68	0.73
p-TOMCAT	0.89	0.81	0.58	0.58
STOCHEM-HadAM3	0.88	0.88	0.66	0.68
STOCHEM-HadGEM	0.89	0.85	0.63	0.66
TM4	0.80	0.89	0.44	0.67
TM5	0.71	0.88	0.29	0.59
ULAQ	0.58	0.66	0.39	0.48
UM-CAM	0.87	0.74	0.49	0.55
Multimodel average	$0.84~\pm$	$0.83 \pm$	$0.55 \pm$	$0.61 \pm$
	0.08	0.07	0.11	0.07

^aCorrelations (Pearson's) are derived using model fields sampled with MOPITT April 2001 and October 2000 averaging kernels and a priori CO profiles and MOPITT observations from those same months (i.e., single year measurements).

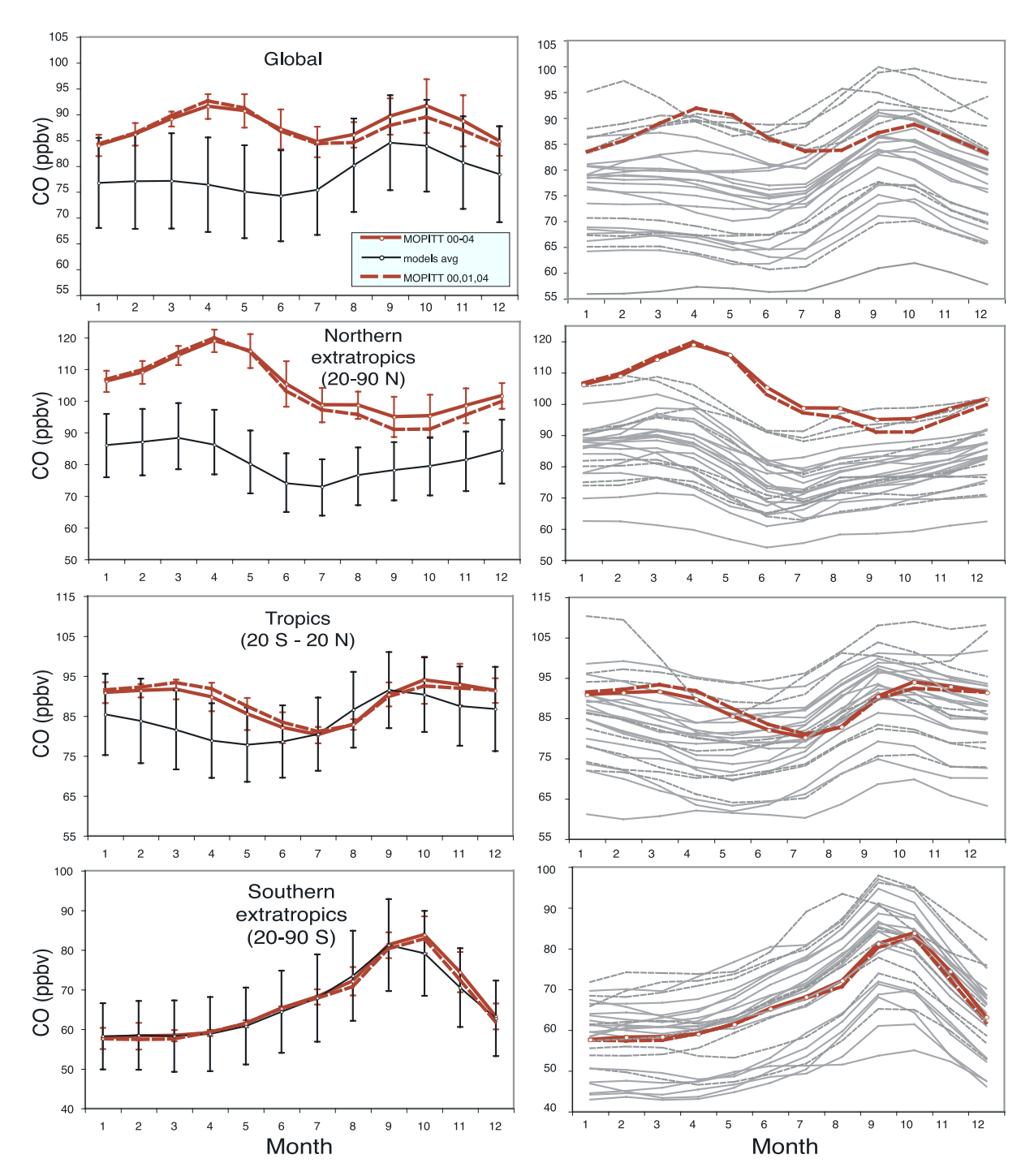


Figure 3. Annual cycle of CO in observations and in the models for the MOPITT 500 hPa retrieval level. MOPITT data (red) include averages over the entire 2000–2004 period (solid line) and excluding 2002 and 2003 (dashed line), and include the standard deviation over 2000–2004. Model results (black) show the (left) S1 (2000 control) multimodel model mean and standard deviation and (right) results from each individual model, with dashed lines among the individual models indicating those models with methane lifetimes outside the TAR range.

 $\sim \! 10$ ppbv lower than any of the others). The five models with the largest CO are those with a methane lifetime longer than the TAR recommended range (Table 1). Those models with a methane lifetime shorter than the TAR range are

among the lower models, but do not stand out as distinctly from the other models. Excluding these "outlier" models has little effect on the multimodel mean results for either the global or regional averages.

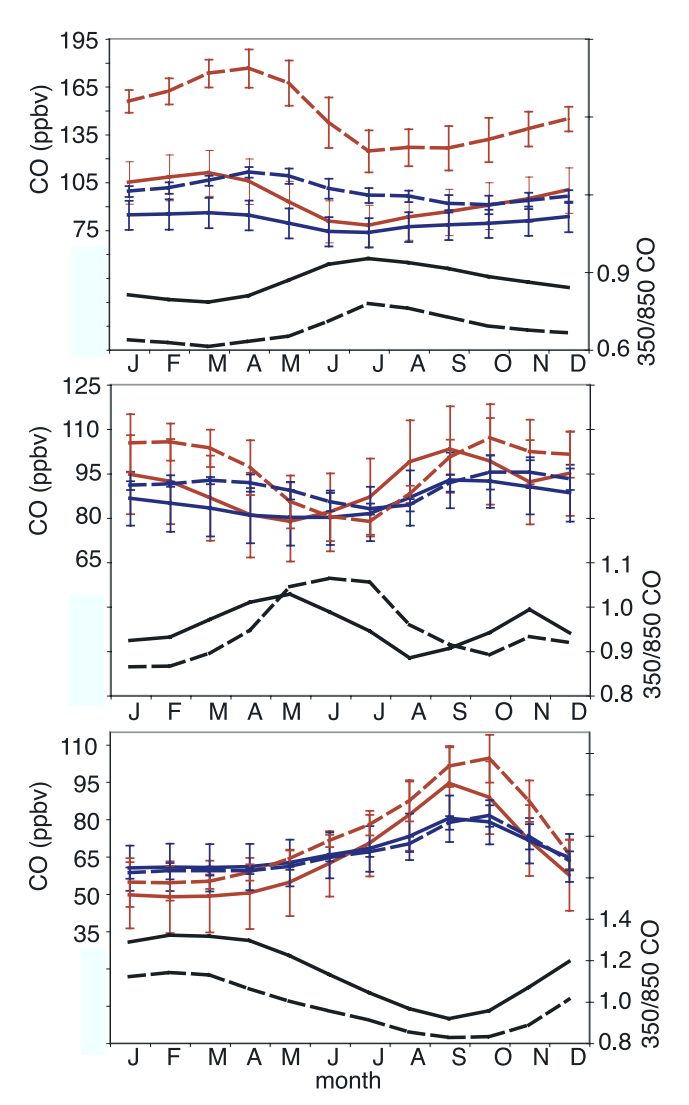


Figure 4. Annual cycle of CO in observations (dashed) and for the S1 (2000 control) model simulations (solid) as in Figure 3 but for the MOPITT 350 (blue) and 850 hPa (red) retrieval levels and their ratios (black). Annual cycles are shown for the (top) NH extratropics (20–90°N), (middle) the tropics (20°S–20°N) and (bottom) the SH extratropics (20–90°S).

[21] Looking at the results averaged zonally over the extratropics and the tropics makes it clear where the global biases stem from. The northern extratropics are the primary source of the boreal springtime maximum in global mean CO, and it is in this area that the models perform most poorly (Figure 3, second row). Not a single one of the 26 models simulates as much CO as in observations during March through July. The only models that reach the observed abundance levels during any months are those with methane lifetimes longer than the TAR range. The discrepancies in April discussed previously are clearly by no means unique, but rather are representative of the entire boreal spring. Similarly, the October differences are representative of those seen from August through February. Exclusion of 2002 and 2003, years with elevated boreal burning, has little effect on the MOPITT averages, especially during the boreal spring.

- [22] In the tropics (Figure 3, third row), many of the models do a better job, though the seasonality is typically shifted one to two months early in the simulations. The standard deviation of the models encompasses the observations in all but one month. Again the model results are for the most part relatively continuously distributed. The ULAQ model is again the lowest by a substantial margin, while during boreal winter STOCHEM HadGEM is substantially larger than the others. In the southern extratropics, the multimodel average is in remarkably good agreement with observations (Figure 3, bottom left). In this region, all but one model (STOCHEM HadGEM) simulates the seasonal maximum at the same or within one month of observations (Figure 3, bottom right). However, even in this region the individual models show CO values that vary by more than a factor of two and there is no evidence of a clustering of results near the measured values. Instead, a large group of models has values roughly 5-15 ppbv too big, while a smaller group has values 15-20 ppbv too small, leading to a fortuitous multimodel average agreement with observations.
- [23] The patterns of the model/MOPITT CO comparisons are similar at other vertical levels (Figure 4). In the NH extratropics, the underestimate of CO in the models is present at all levels, not only the broad midtropospheric 500 hPa retrieval level. Similarly, the models are generally in reasonable agreement in the tropics and SH extratropics, with comparable biases in tropical seasonality to those seen at 500 hPa. Consistent with these results, there is no significant difference between the models' spatial correlations at different vertical levels (Table 4). Differences in all regions generally decrease with height above the surface, as in an earlier CO model intercomparison with aircraft data [Kiley et al., 2003]. The ratio of 350/850 hPa retrieval level CO is uniformly greater in the models than in observations in the extratropics. This is not the case in the tropics, however, where the magnitude of the ratio is in good agreement with observations though again the seasonality is off by 1-2 months. Model overestimates of the strength of extratropical convection could account for the extratropical biases, as could an underestimate of direct CO surface emissions relative to indirect production from hydrocarbon oxidation aloft. Note, however, that there is little vertical information in the extratropics [Deeter et al., 2004].
- [24] The variations between the tropics and extratropics can also be examined in terms of the ratios between the CO in these regions. We focus on the boreal summer, when the average model tropical CO is within the standard deviation of the MOPITT data and the northern extratropical bias is large. Observations indicate that during these months, SH extratropical mean CO is substantially less than the tropical mean, while NH extratropical mean CO is greater. The models perform reasonably well in matching the observed decreased CO in the southern extratropics relative to the tropics, with an average of 16.5% less CO in the south versus 16.2% in observations, though the models exhibit a wide range of values (Figure 5). Comparing the northern extratropics to the tropics, nearly all models exhibit a ratio of less than one, in contrast to observations. Only two models show more CO in the northern extratropics, and even these show enhancements of only 1 and 4% while the observations show 24% more CO in the northern extra-

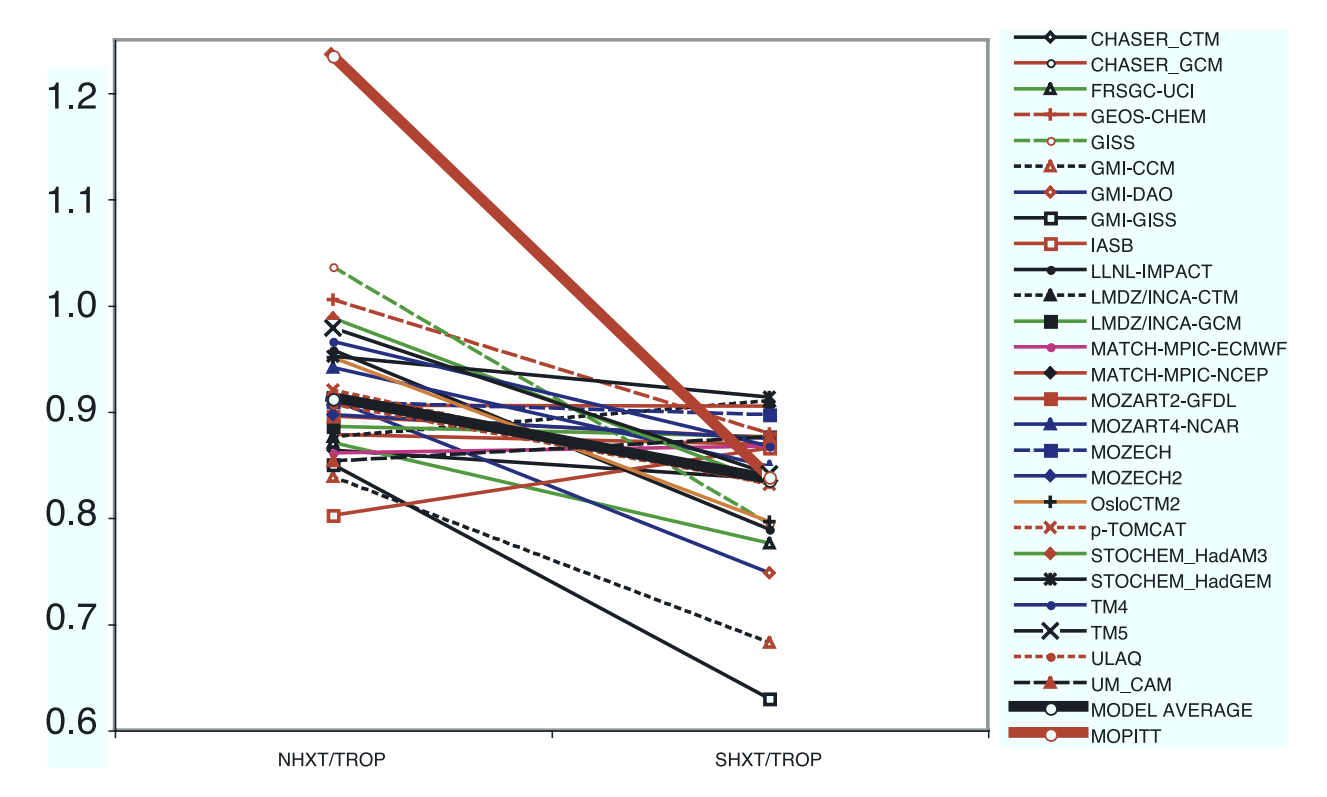


Figure 5. June-August average ratio of extratropical to tropical mean CO for the MOPITT 500 hPa retrieval level in models and in 2000–2004 observations. (NHXT, NH extratropics (20–90°N); SHXT, SH extratropics (20–90°S); TROP, tropics (20°S–20°N)). The slope of the line shows the gradient between the two extratopical regions. MOPITT values excluding 2002 and 2003 are 1.20 for NHXT/TROP and 0.82 for SHXT/TROP (these are 1.24 and 0.84 for the full data set).

tropics. Surprisingly, a few models actually show less CO in the NH extratropics than in the SH extratropics (IASB, LMDz-INCA-CTM, MATCH-MPIC-ECMWF and UM_CAM), suggesting that they may have excessive OH in the polluted NH extratropics.

[25] As shown previously (Figure 4), model biases in comparison with MOPITT are substantially larger in the lower than the middle/upper troposphere in the NH extratropics. The large differences in the lower troposphere are consistent with comparisons between the multimodel average and GMD surface observations. These show extremely large negative biases in the models at high northern latitudes (Barrow, Alert), especially during the boreal spring when they typically exceed 50 ppbv (Figure 6). These decrease to smaller, but still substantial negative biases in CO amounts at northern midlatitudes. The models also have difficulties in reproducing the seasonal cycle correctly at some locations. Comparisons at Mauna Loa (20°N) show better agreement during NH summer, but continue to exhibit negative model biases during NH late winter and early spring. Most models do an excellent job of capturing the observed annual cycle at Samoa (14°S). For the SH, models again capture the seasonal cycle well at Cape Grim (41°S), but nearly all show a positive bias year-round. Thus as in the MOPITT-model comparisons, agreement is substantially better in the tropics and SH than in the NH extratropics, and the negative biases exhibited by the models in the NH extratropics are generally largest during boreal spring. Comparison of large model grid boxes with remote station

data will generally contribute a positive model bias by incorporating nearby emissions (except over extremely remote locations such as mid-ocean islands, where it should have little effect). Additionally, the GMD monthly mean values exclude "nonbackground" data, which is not done in the models. This would also bias the model values high, and thus cannot account for the discrepancies shown here (Figure 6).

[26] The surface CO simulations in the models are often quite similar to one another. Resolution differences will play some role in the differences, as coarser models will tend to have more emissions in the grid boxes containing the remote sites. A distinct correlation with resolution is not obvious though. It is useful to examine the outlying models in the comparisons for similarities. We focus on positive outliers, as most models show similar negative biases in the NH (the exception is the ULAQ model, which is significantly lower than the others at all NH sites except Niwot Ridge during spring). At both Niwot Ridge and Tae Ahn, several models clearly depart from the other models (Figure 6). At Niwot Ridge, many models have a poor representation of seasonality, and three stand out with a July-September maximum and CO values greater than 130 ppbv during the peak month of August (GMI/CCM 154 ppbv, GEOS-CHEM 139 ppbv, and GMI/GISS 133 ppbv) while observations show a value of 100 ppbv. At Tae Ahn, five models give June values more than one standard deviation greater than the observations (TM4 398 ppbv, MATCH-MPIC-NCEP 352 pbbv, FRSGC 301 ppbv, GEOS-CHEM

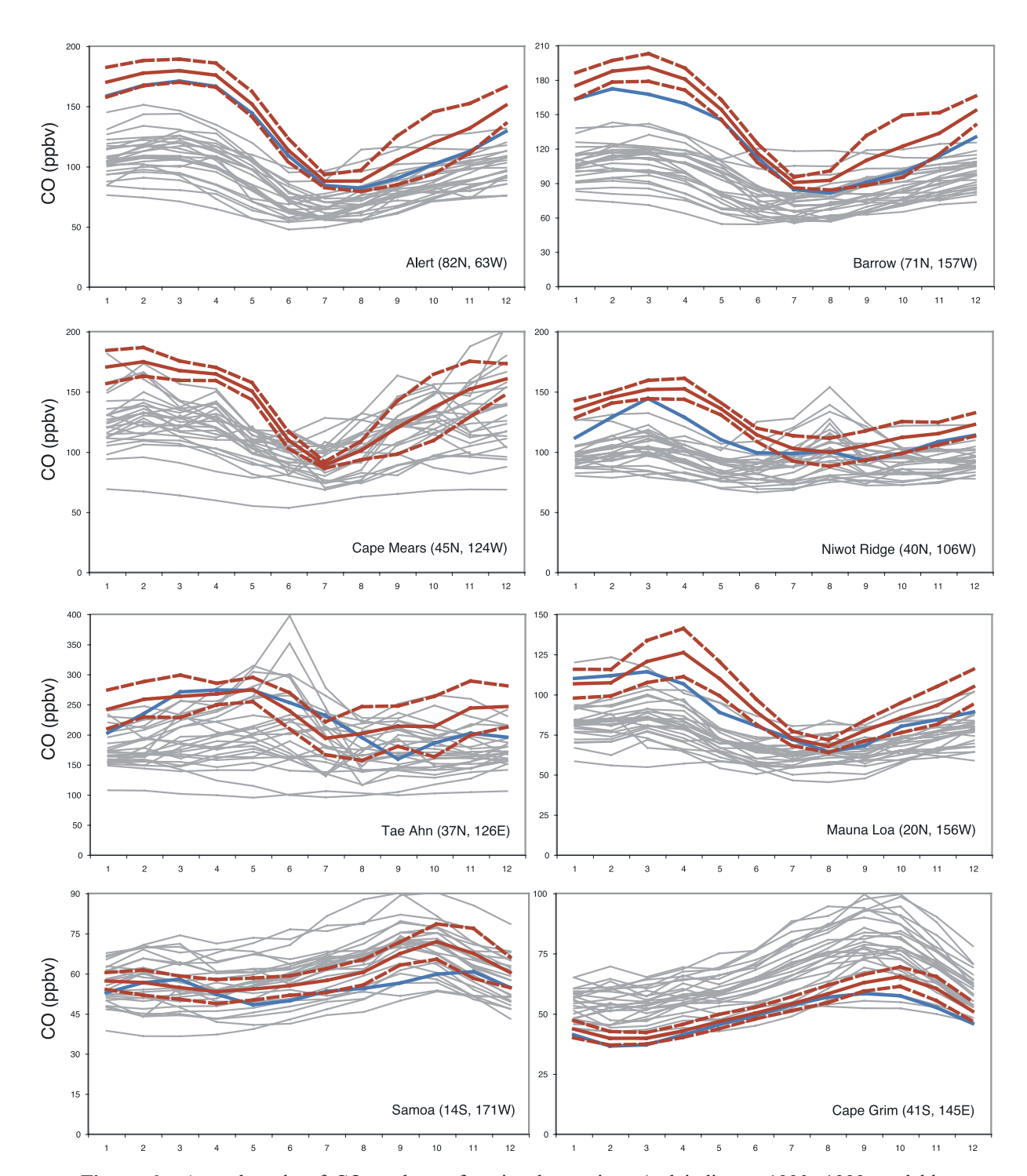


Figure 6. Annual cycle of CO at the surface in observations (red indicates 1990–1999, and blue indicates 2000) and for individual models (black). Model values are from the lowest layer, except for the high-altitude sites of Mauna Loa and Niwot Ridge. For the observations, solid lines show monthly mean values and dashed lines the standard deviation. Observations are from the NOAA GMD network [Novelli et al., 1998]. The numbers along the horizontal axis give the month.

299 ppbv, MATCH-MPIC-ECMWF 295 ppbv) which show just under 240 ppbv for the 1990s average and 253 for 2000. Note that both sites are close to source regions, so are sensitive to grid box size and location as well as boundary layer mixing. However, of these 8 positive outliers, all were single year

CTM runs, suggesting the meteorological variability could have played a role in these high values (though not all CTMs using these meteorological fields were outliers, and so other factors must also contribute). This is further supported by the fact that alternative meteorological fields used with the same

models produced quite different values: GMI/DAO was 40 ppbv less than GMI/CCM at Niwot Ridge, while MATCH-MPIC-ECMWF was 57 ppbv less than MATCH-MPIC-NCEP at Tae Ahn). This suggests that at least for species such as CO that are subject to long-range transport, single year CTM integrations are not adequate for climatological comparison with point measurements. The results also suggest that potential differences between meteorological fields from different meteorological centers or analysis products may be important for simulating long-range transport events.

[27] Examining the spread of model results at other locations, there are clearly problems with seasonality in addition to those noted at Niwot Ridge. At Barrow (Figure 6), two models simulate CO values more than one standard deviation above the observations during the July-August minimum (MOZART4-NCAR and GEOS-CHEM). Closer examination reveals that the seasonal cycle is much too weak in these models (and in several others with lower overall values). At Cape Mears, the CHASER-GCM, IASB, MOZECH2, STO-CHEM-HadAM3 and ULAQ models all have seasonal cycles that are nearly flat or are almost completely out of phase with the observations, while the related CHASER-CTM, MOZECH and STOCHEM HadGEM models perform much better. At least at the stations discussed thus far, differences in meteorology thus appear to have large effects. In contrast, most models do a good job of reproducing the observed seasonality at Alert, Mauna Loa, Samoa and Cape Grim, though the amplitude is sometimes too weak. Even at Cape Grim, however, several models peak earlier than the October peak in the observations. The STOCHEM-HadGEM model peak in August, while the ULAQ model peaks in June. Interestingly, the STOCHEM-HadGEM comparison with MOPITT in the SH extratropics shows a similar early peak (Figure 3, fourth row), however the STOCHEM-HadAM3 comparison does not. Together, these results suggest that great care must be taken when evaluating global models using limited, isolated station data, even for CTMs using assimilated meteorological fields. As most of the models that stand out as outliers in comparison with the surface measurements do not stand out when compared with the broader satellite coverage (Table 4), these results also highlight the value of the satellite observations in extending the data available for model evaluation beyond a small number of remote sites subject to large variations due to meteorology.

4. Discussion of Present-Day Results

[28] The negative biases in the NH are present from the surface upward throughout the upper troposphere, indicating that the biases do not merely reflect an erroneous vertical structure of CO in the models. Instead, the results strongly suggest that the CO sources used in the simulations are too small in the NH extratropics. NMVOCs also contribute indirectly to CO via oxidation, and there is also the possibility that these sources contribute to the underestimates in this region. It seems less likely that flaws in the chemical mechanisms account for much of the negative bias, as these would generally not be expected to be specific to the NH extratropics. A possible exception are uncertainties in the degradation of some industrial NMVOC com-

pounds produced primarily in the NH extratropics, as details of the full pathways are not well known.

[29] The distribution of CO produced from oxidation of methane may also be slightly biased. The models used a prescribed methane loading of 1.76 ppmv everywhere, while surface observations from the NOAA GMD network during the early 2000s show values of \sim 1.7 ppmv in the SH extratropics, and \sim 1.85 in the NH extratropics (*Dlugokencky et al.* [1994], updated at http://www.cmdl. noaa.gov/ccgg/iadv/). These effects are likely to be quite small, however.

[30] Given that the models' negative biases are greatest during boreal spring (Figure 3), an underestimate of CO emissions from NH biomass burning seems a potential candidate. The small difference between the MOPITT analyses including and excluding the elevated burning years of 2002 and 2003 argues against boreal burning accounting for the bulk of the model negative biases, however. It appears that models do not adequately capture CO accumulation during the OH-poor winter. They also do not include a seasonal cycle in methane, which may contribute to the underestimate of the springtime maximum in CO in the NH when the winter buildup of methane is oxidized (though it is unlikely to play a sizable role in winter itself). It is also probable that some of the underestimate stems from not including seasonality in anthropogenic emissions other than those from biomass burning. Inverse modeling results indicate that the seasonality of fossil fuel burning CO emissions may be about 15%, with enhancements taking place during the correct time of year to increase the springtime NH extratropical CO [Pétron et al., 2004]. Along with seasonal emissions, a year-round underestimate of emissions from east Asia is indicated by the failure of models to reproduce the observed large CO values seen there and in downwind locations over the Pacific during all seasons (Figure 2). Such a result implicates emissions from fossil fuel burning. This interpretation is consistent with inverse modeling indicating that larger sources are needed to account for atmospheric measurements. For example, while this intercomparison used a value for global direct emissions of CO of 1077 Tg(CO)/yr (Table 3), recent inverse modeling studies using both surface and satellite data have consistently suggested larger values ranging from 1228-1694 Tg(CO)/yr [Arellano et al., 2004; Bergamaschi et al., 2000; Pétron et al., 2002, 2004] (though large uncertainties in the indirect source of CO from NMVOCs also influence the reliability of the inverse modeling results). The underestimate of east Asian CO emissions in the IIASA national estimate-based inventory is also consistent with underreporting of NO_x emissions inferred from satellite/model comparisons of NO₂ [van Noije et al., 2006], and with recent inverse modeling [Heald et al., 2003; Palmer et al., 2003] and "bottom-up" [Tan et al., 2004] calculations focusing on Asian emissions. We note also that the TAR simulations, using nearly 50% more direct CO emissions, generally matched the surface CO observations better than the current model simulations (with the exception of Cape Grim, where a positive bias has been reduced owing to the lower emissions).

[31] Since tropospheric CO is relatively long lived, especially in the extratropics and during the winter months, deficiencies in model transport could also play a role in the

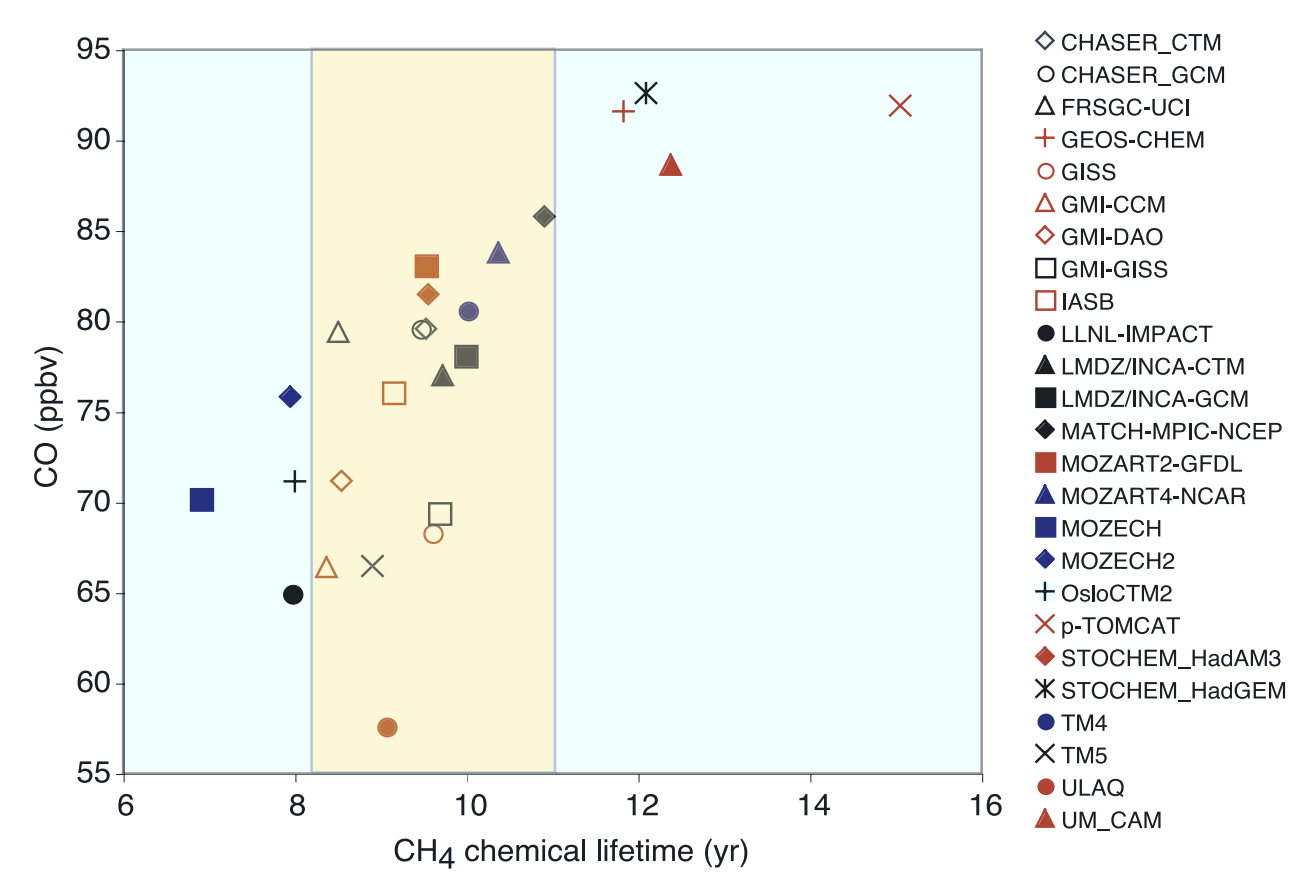


Figure 7. Annual average methane chemical lifetime (inversely proportional to OH) versus CO in the broad 500 hPa MOPITT retrieval level. The shaded area indicates the TAR lifetime derived from observations and modeling.

NH underestimate of CO. The potential magnitude of uncertainties in meteorology can be assessed by comparing CTMs driven with multiple meteorological fields. For example, the March-May northern extratropical bias in the multimodel mean is -29 ppbv. The two MATCH simulations using different assimilated meteorological fields differ by 5 ppbv, while the three GMI simulations using model-derived or assimilated meteorological fields differ by 8 ppbv. It thus seems quite unlikely that meteorology could play more than a minor role in the systematic model underestimates of the extratropical mean value during northern spring.

[32] It is of course also possible that the models' CO sink is too strong. While the global distribution of OH has not been directly measured, methylchloroform observations do constrain tropospheric oxidation rates, and indicate that methane's chemical lifetime is in the range of 8.2-11.0 years [Prather et al., 2001]. The mean model result of a 9.7 (±1.7) yr methane chemical lifetime is in good agreement with this range, suggesting that the sink is not generally overestimated (Figure 7). Note that the oxidation of methane is not a perfect analogue for CO, as the reaction of CO with OH is not temperature-dependent while that of methane is, making it most sensitive to OH in the tropical lower troposphere. However, it is nevertheless a reasonably good proxy (as discussed below). Biases in the sink strength do affect the results of some models. While the multimodel mean underestimates CO, four models have global mean

500 hPa retrieval level CO values as large or larger than MOPITT's value of 87.2 ppbv (Table 1). These models (GEOS-CHEM, pTOMCAT, STOCHEM-HadGEM, and UM_CAM) all have such large values at least in part because their methane chemical lifetimes appear to be substantially too long (11.8–15.1 years, Figure 7), indicating that their OH values are too small.

[33] The spread in model results, both globally and regionally, is quite large. Since the models all used identical methane abundances and CO emissions, other factors must be responsible for this large range. We first examine the role of OH variations among the models. Oxidation of CH₄ and other hydrocarbons by OH is a major source of CO, while reaction with OH is also the primary sink for CO. As OH changes, the change in the sink of CO dominates, so that the abundance and lifetime of CO should be inversely proportional to OH (as for methane and methylchloroform, as discussed above). The inverse correlation between global mean mass-weighted OH and CO in the models, using the broad 500 hPa MOPITT retrieval level as representative of the overall tropospheric CO burden, is quite high (R = 0.80). Leaving out the most outlying models, ULAQ, OsloCTM2 and pTOMCAT (Table 1) increases the correlation to R = 0.88. Thus the variation in OH explains nearly 80% of the intermodel variance in CO. Values are similar using the CH₄ lifetime, which shows a correlation with the same CO analysis of R = 0.75 for all models. The similarity arises because the methane lifetime is highly correlated with

Table 5. Indirect Sources of CO in the Models^a

	Total CO Chemical Production	CO From Methane Oxidation	CO From NMVOC Oxidation	CO Yield From Methane
FRSGC UCI	1746	886	860	0.86
GISS	1265	633	632	0.82
IASB	nr	nr	657	0.93
LLNL-IMPACT	1565	999	566	0.87
MATCH-MPIC-NCEP	1543	737	806	0.93
STOCHEM-HadAM3	1918	720	1198	0.77
STOCHEM-HadGEM	1422	578	844	0.81
TM5	1282	820	462	0.82
ULAQ	1301	754	547	0.91
Multimodel mean	1505	766	730	0.86
Standard deviation, % of mean	236 (16%)	135 (18%)	224 (31%)	0.06 (7%)
Spread, % of mean	653 (43%)	421 (55%)	736 (101%)	0.16 (19%)

^aUnit of CO is Tg CO/yr. The yield from methane represents the fraction of carbon from methane that is eventually oxidized to CO rather than being removed while in a more reduced state. An additional five models reported total CO chemical production. Including those results, the multimodel mean becomes 1545 Tg CO/yr, with a slightly reduced standard deviation of 193 Tg CO/yr.

the global mean OH (R = 0.92 for all models except OsloCTM2), indicating that the methane lifetime, which can be constrained from observations of methylchloroform as they have quite similar temperature sensitivities, is indeed quite a good proxy for global OH.

[34] We also calculated global mean OH weighted by the local CO+OH rate coefficient (Table 1). In nearly all models, this increased the OH by $0.1-0.3 \times 10^5$ molec cm⁻³. The only exceptions were the GMI and GISS models, which showed no change or in one case, a slight decrease. This stems from those models placing the OH maximum generally higher in altitude than other models. The correlation between OH and CO is nearly identical using this weighted OH value (R = 0.79 for all models), however.

[35] Interestingly, though the correlation between the modeled ozone burdens and OH is fairly high (0.63), the standard deviation and spread of OH values is greater than the standard deviation and spread of ozone burdens (Table 1). These results imply that part of the variance in OH arises from intermodel differences in factors such as water vapor abundances, photolysis of ozone to O(¹D), or removal of OH (rather than in ozone abundance alone). That these factors should vary amongst models is not surprising given that the hydrological cycles are treated very differently in the various CTMs and GCMs, and this can have large impacts as more efficient removal of soluble species will decrease reactive nitrogen, reducing O₃ and hence OH production, and also increases removal of HO_x (via H₂O₂) further reducing OH. Likewise, the photolysis of tropospheric ozone at wavelengths of ~310 nm and shorter and the quantum yield of excited oxygen are extremely sensitive to differences in the photolysis schemes used, including their interaction with clouds, and to the overlying ozone prescribed in the stratosphere. The variation among modeled OH amounts is also related to differences in the rate at which HO₂ is recycled to OH. This portion should be strongly related to the intermodel variations in the tropospheric NO_x and ozone burdens.

[36] The global mean values of CO show reduced standard deviation and spread in comparison with OH (Table 1). This may occur partially because OH is most abundant in the tropics while CO is most abundant in the NH extra-

tropics. Probably of greater importance, however, is that increases in OH not only reduce the lifetime of CO, but also increase production of CO from methane. The indirect source of CO from NMVOC oxidation also contributes to wide range of simulated CO. This would not be equal among models even if they all had the same OH, since the models include different representations of both which NMVOCs are considered and their oxidation pathways, as noted previously. Additionally, while the intercomparison protocol suggested specific emissions of NMVOCs, some models estimated biogenic NMVOC emissions using internal climate-sensitive schemes, leading to large difference in total emissions.

[37] To examine the role of intermodel differences in CO chemical production, we analyzed the oxidation of methane and NMVOCs (Table 5). While not all models were able to provide these diagnostics, there is sufficient sampling to provide meaningful correlations and to characterize variability. For the multimodel mean, the CO produced from the oxidation of methane and NMVOCs is quite similar, at 766 and 730 Tg CO/yr, respectively. These were estimated as 800 and 430 Tg CO/yr in the TAR [*Prather et al.*, 2001], which assumed only 220 Tg C/yr emissions of isoprene. Hence in the current study, the indirect source of NMVOCs is substantially larger and compensates for much of the difference in direct emissions relative to the TAR (though the total direct plus indirect sources here are still ~200 Tg CO/yr less than in the TAR).

[38] While all models had identical methane fields, there is substantial variation in the CO source from methane oxidation owing to differences in the simulated OH and in the yield of CO, which varied from 0.77 to 0.93 across the models. Models with lower CO production from methane oxidation have generally greater CO amounts, though the correlation is weak (R = 0.45). Both effects presumably reflect more efficient removal of soluble species, with removal of hydrocarbon intermediates reducing the CO yield from methane and wet removal also reducing the reactive nitrogen precursors of ozone and OH as well as the H_2O_2 reservoir for OH (as noted previously). Thus variations in the CO production or yield from methane oxidation do not directly account for the intermodel differences in CO.

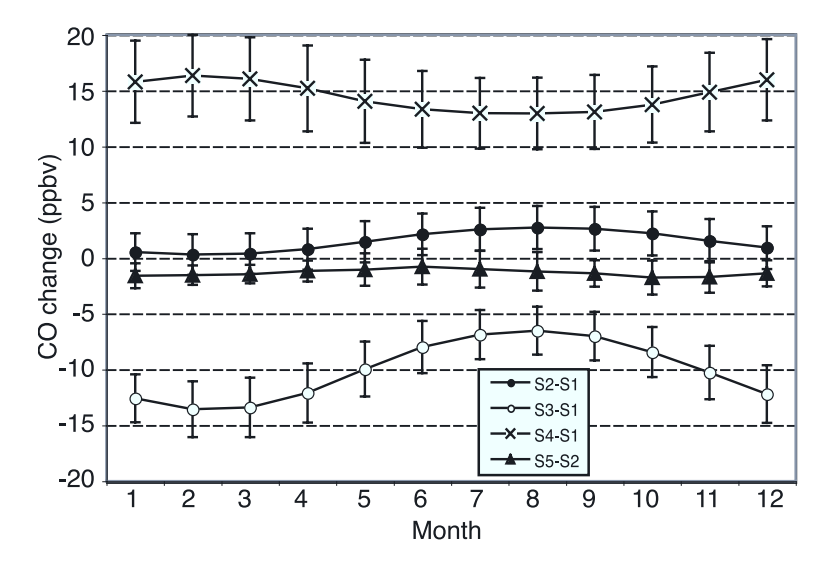


Figure 8. Annual cycle of global mean changes in 850 hPa CO in the future simulations relative to the present due to emissions (S2-S1:CLE, S3-S1:MFR, and S4-S1:A2) and due to climate change (S5-S2). Error bars show the standard deviation among the models.

In contrast, the CO production from NMVOC oxidation shows a strong positive correlation with tropospheric CO amounts (R = 0.70). Not surprisingly, the variation across models in the production of CO from NMVOCs is quite large, with differences as high as a factor of two. Variation in the indirect source of CO from methane oxidation are less than those for NMVOCs, though still fairly large, and are more closely coupled to variations in model OH than to differences in the yield of CO (though these are of course not independent). Thus an overall picture emerges in which variations in OH, augmented by variations in NMVOC representation (which play a role in creating the OH variations), play the largest roles in creating the large intermodel CO differences.

[39] Intermodel variations in transport may play some role as well. Excessive transport from the extratropics into the tropics, with greater OH, could conceivably reduce the global CO burden, for example. It is not possible to diagnose this transport from the fields submitted as part of the intercomparison, but this is worthy of future attention. However, it would be a surprising coincidence if the model transports were quite unrealistic and yet the models generally matched the ratio of southern extratropical to tropical mean CO (Figure 5).

[40] Since intermodel variations in ozone seem responsible for a great deal of the variations in OH that in turn affect CO, an obvious question is why is the intermodel variation in ozone so large? Again, the representation of NMVOCs is different in each model, so that the sources of ozone precursors are not identical. Lightning NO_x also varies between models, as many generate this internally, though other NO x sources are identical. However, differences in NO_x removal may nevertheless lead to substantial variations in the NO_x burden among models. As shown in the discussion of intermodel ozone differences by *Stevenson et al.* [2006] there is also a substantial variation in the influx of ozone from the stratosphere, with models reporting a range of 151 to 930 Tg O₃/yr (multimodel mean 552 \pm 168 Tg O₃/yr). This leads to especially large differences

in ozone fields in the upper troposphere, which have less influence on OH, but can also affect lower altitudes. Finally, differences in the strength of the hydrologic cycle, which removes soluble gases and can efficiently transport pollution out of the boundary layer, likely play a major role in the intermodel ozone differences. As cloud physics is one of the most uncertain aspects of climate modeling, this is an area where reductions in uncertainties are likely to take place quite slowly.

5. Future CO

[41] We now examine the change in CO projected by the models in response to future emissions and future climate. Since not all models performed all simulations, comparisons include only models with simulations for both present-day and future conditions for a given scenario, and in the case of climate change, models that simulated 2030 conditions under the CLE scenario both with and without projected climate changes. All model analyses are performed at fixed pressure levels (rather than the MOPITT retrieval levels used previously).

5.1. Effects of Emissions

[42] The response of CO to changes in emissions is highly dependent upon the scenario used. For the 850 hPa global average, the CLE scenario (S2) causes little change in CO, while the MFR (S3) and A2 (S4) scenarios cause substantial (10–20 ppbv) decreases and increases relative to the year 2000 (S1), respectively (Figure 8). Changes tend to be largest in the MFR and A2 scenarios during boreal winter and spring, and in the NH extratropics (Figure 9). Changes at higher altitudes show almost identical annual cycles but with decreasing magnitude (e.g., changes at 500 hPa are $\sim\!\!2/3$ the 850 hPa changes) for both the global and regional analyses of all three scenarios.

[43] The distribution of CO changes in the 2030 simulations is extremely inhomogeneous geographically, however, so that the zonal averages fail to capture much of the

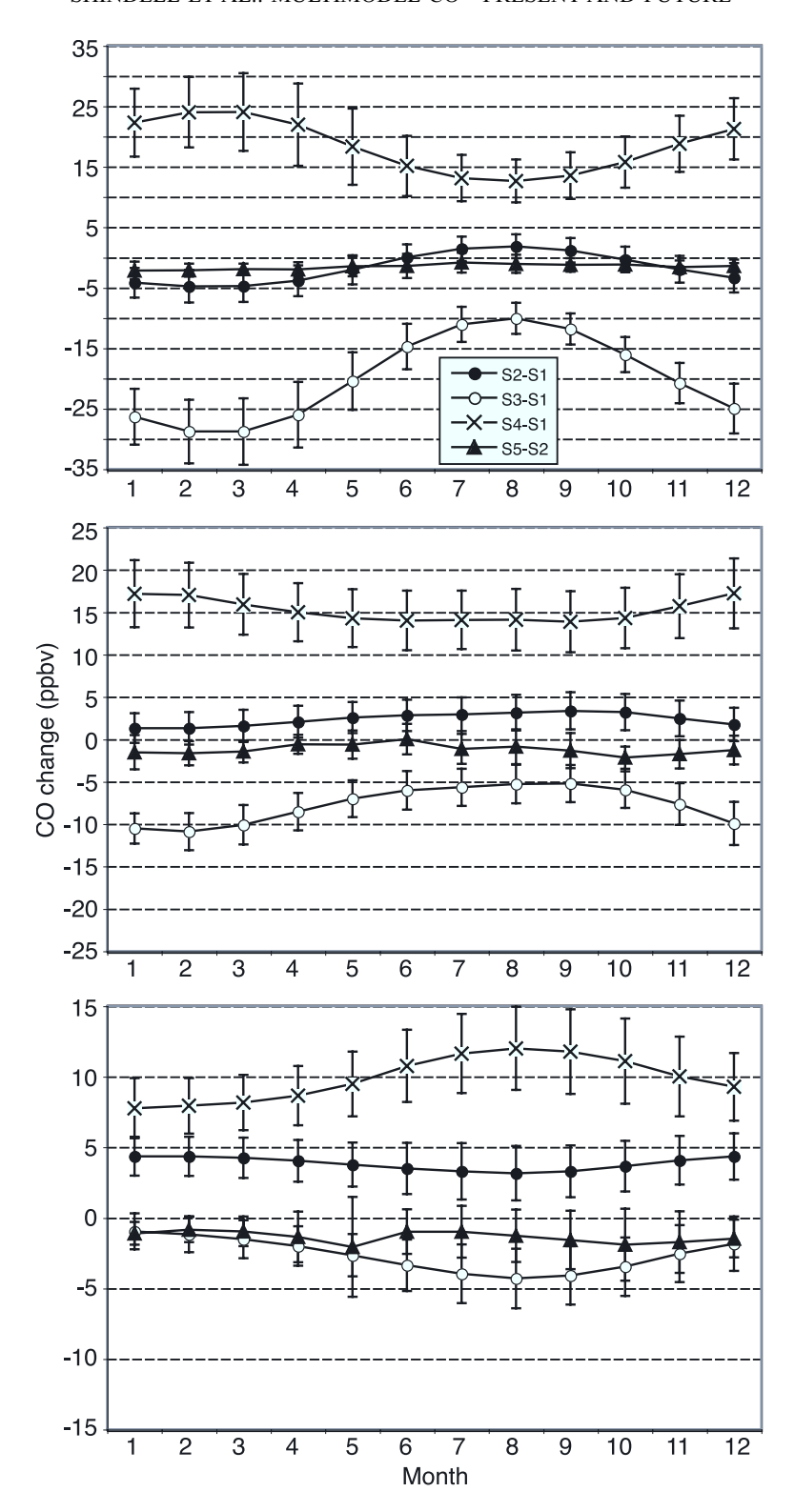


Figure 9. Annual cycle of changes in 850 hPa CO as in Figure 8 except for (top) the NH extratropics, (middle) the tropics and (bottom) the SH extratropics.

complexity of the CO projections. In the interest of space, we examine the worldwide distribution of modeled changes by again focusing primarily on April and October and on the 500 and 850 hPa levels. As in our earlier analyses, these are broadly representative of the changes during the two halves of the year. During April, the models show an

increase in CO from about 10°N to 90°S in the CLE simulations for the 850 hPa level, and decreases in the NH extratropics, with pronounced regional inhomogeneity (Figure 10). In the middle troposphere, the pattern is similar but much of the regional inhomogeneity has been smoothed out. In the MFR simulations, the models show minimal

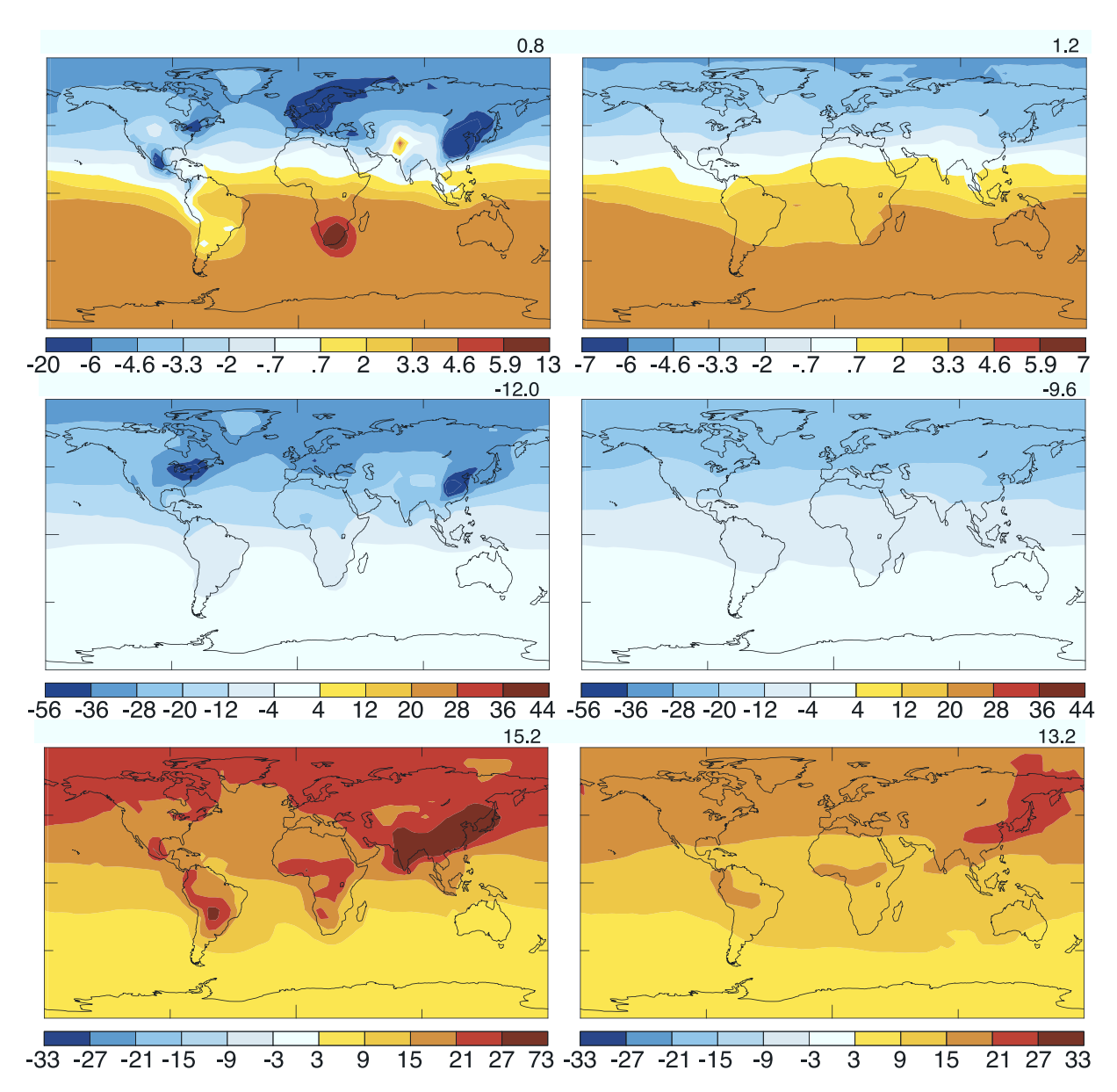


Figure 10. Changes in April CO (ppbv) relative to the present-day for 2030 conditions under (top) the CLE, (middle) the MFR and (bottom) A2 scenarios. (left) The 850 hPa level and (right) the 500 hPa level. Values at the top right corner of each plot give the area-weighted global mean change. Note that scales vary between rows.

changes in the SH, and large reductions in the NH, especially in the extratropics, with decreases exceeding 35 ppbv over the NE US/SE Canada and east Asia near the surface. The A2 scenario leads to CO increases everywhere, with near-surface CO elevated by more than 10 ppbv over all the continents except Australia, and especially large increases of up to 70 ppbv over south and east Asia. These latter increases are so large that they can still be seen as regional enhancements at 500 hPa over and downwind of the Asian source regions (Figure 10).

[44] The future CO changes are qualitatively similar in October, but typically with a reduced magnitude in comparison with April as chemical destruction of CO is more rapid closer to boreal summer (Figure 11). In the CLE simulations, Indonesia and southern Africa are hot spots for CO increases

at 850 hPa. The general decrease in NH extratropical CO is so small that it does not reach 1 ppbv anywhere by 500 hPa. The MFR simulations show CO reductions of more than 20 ppbv at 850 hPa over the industrialized regions of the NH, and relatively homogeneous reductions of 10–15 ppbv at 500 hPa. The A2 simulations show increased CO worldwide, and as in October the largest values are over south and east Asia (up to 70 ppbv at 850 hPa).

[45] The large regional changes in near-surface CO discussed above are quite robust across models, with most responses being highly significant (Table 6). While the model results are typically distributed fairly normally, there is some skewness to the MFR results over the NE US and SE Canada, with considerably larger decreases than the mean being relatively more probable. This results from

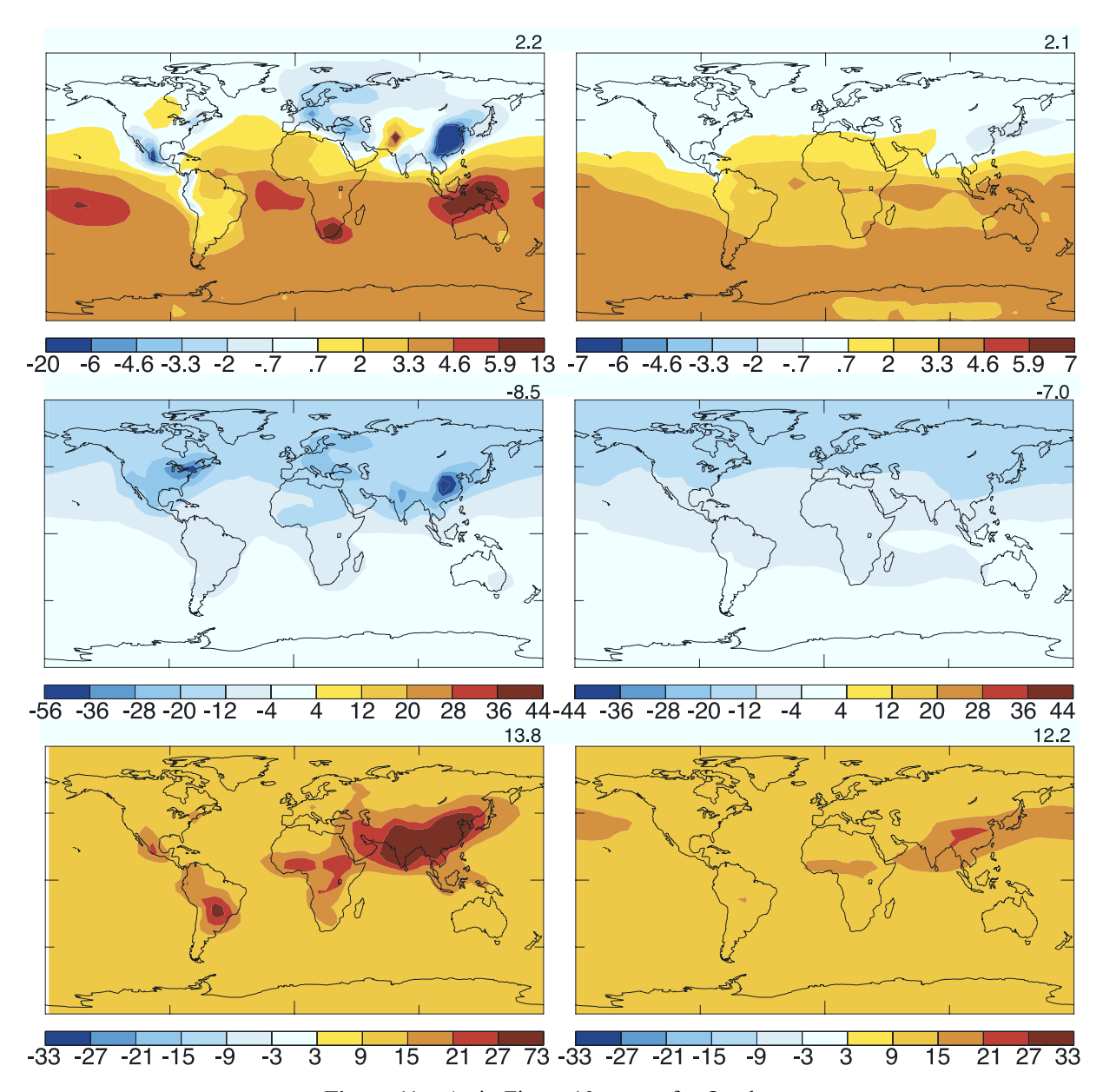


Figure 11. As in Figure 10 except for October.

three models (TM4, GEOS-CHEM, and GISS) showing roughly a factor of two greater response than the other models. While these models stand out somewhat in this region in the other scenarios as well, the differences are less stark and the models do not stand out in other areas. Thus the reason for these differences is not clear. At higher levels, variability is even less, so that the 500 hPa responses over the NE US and SE Canada, for example, were -1.0 ± 2.0 for CLE, -16.7 ± 3.3 for MFR, and 15.5 ± 4.8 for A2. Thus

for the regions with large CO responses to future conditions, the difference between emission scenarios is much larger than the difference between models.

[46] It seems clear that the bulk of the projected changes in atmospheric concentrations result from changes to the sources of CO rather than change in its removal. Changes to OH in the scenarios, as diagnosed from changes to the methane removal rate, were +3.1% for CLE, +1.0% for MFR, and +0.3% for A2. The resulting changes in oxidation

Table 6. Regional 850 hPa Annual Average CO Response to 2030 Emissions^a

Region	CLE Mean	CLE Range	MFR Mean	MFR Range	A2 Mean	A2 Range
NE US and SE Canada	-3.2 ± 3.5	-4.0 to -11.4	-38.0 ± 17.7	-91.5 to -22.7	17.7 ± 5.7	5.7 to 28.6
Northern Europe	-4.4 ± 2.4	-10.3 to 0.4	-24.7 ± 3.5	-18.3 to -31.5	17.3 ± 5.3	5.3 to 25.4
East Asia	-9.5 ± 3.7	-3.4 to -17.0	-35.2 ± 6.2	-21.6 to -47.3	42.4 ± 7.3	31.9 to 58.8

^aRegions are defined as follows: NE US and SE Canada is $40-50^{\circ}$ N, $270-290^{\circ}$ W, northern Europe is $40-60^{\circ}$ N, $0-30^{\circ}$ E, and east Asia is $25-45^{\circ}$ N, $105-125^{\circ}$ E. Unit is ppbv.

of CO would be quite small. Further diagnostics of the OH changes in the simulations (M. Krol, manuscript in preparation, 2006) will show if OH changes in some regions were more important than these very small changes primarily in the tropical lower troposphere.

5.2. Effects of Climate

[47] The effects of projected climate change between 2000 and 2030 on an atmosphere with 2030 projected CLE conditions are seen in a comparison between the S5 and S2 simulations. We remind the reader that these simulations used prescribed methane amounts from a prior climate model run, so do not include intermodel differences in the effects of climate change on methane removal nor do they include potential effects of climate on methane emissions [Gedney et al., 2004; Shindell et al., 2004]. The calculated composition response to climate change also does not include any aerosol indirect effects. The global average multimodel mean response is a decrease in CO of 0.8–1.8 ppbv during all months (Figure 8), with comparable results at all levels. Results are similar for the tropical and extratropical averages (Figure 9). Many of the changes are of marginal statistical significance. This is partially because of substantial intermodel differences. While almost all models showed annual average CO decreases of 1 to 2.5 ppbv at 850 hPa, the two STOCHEM models found increases of 0.4-0.9 ppbv, for example.

[48] Several factors played a role in the CO changes. First of all, the future climate was warmer. In the 10 participating models, the climate projections used had global mean annual average temperature increases in 2030 of 0.3 to 1.0 K (mean 0.6 K). The water vapor response to the increased evaporation in the warmer climate was an increase of 2.2 to 8.0% (mean 4.5%, based on the total tropospheric burden). Increased water vapor enhances the formation of OH radicals from excited oxygen atoms. The production of OH will also be modulated by the availability of excited oxygen atoms, however, which are produced from ozone. In the future climate, the stratospheric influx of ozone increased by 8% in the models performing the climate change simulations, but was in some cases offset by larger increases in the loss rate of odd oxygen (primarily through the OH-forming reaction of excited oxygen with water), leading to changes in the tropospheric ozone burden of either sign in the models [Stevenson et al., 2006]. This is consistent with results from earlier studies showing increases in both the flux of stratospheric ozone to the troposphere and the chemical loss of tropospheric ozone, leading to small net changes in the tropospheric ozone burden [Collins et al., 2003; Zeng and Pyle, 2003]. The effect of increased humidity was the most important climate influence in the mean, so that the net OH change was positive. Consistent with this the methane chemical loss rate increased by 5.1% in the models (despite a 3.6% decrease in methane). Note that methane's oxidation rate also has a relatively strong temperature dependence, so will have increased in response to the warmer climate as well as increased OH. However, the correlation between the water vapor and methane lifetime changes is 0.96 (based on Stevenson et al. [2006]), implying that the altered OH was the dominant driver of methane changes (the correlation between temperature and methane changes was only 0.72).

[49] Increased OH leads to both greater production of CO by hydrocarbon oxidation and faster removal of CO as it is itself oxidized. The relative importance of these two seems to vary among models. There is a substantial positive correlation between the increase in water vapor (a source of OH) and the change in CO (R = 0.59) and an almost equal anticorrelation between change in the tropospheric ozone burden (much of which is via loss to OH) and CO (R = 0.52) across all models. However, most of the correlation depends on the positive CO changes seen in the two STOCHEM models as compared with the decreased CO in all the other models. The STOCHEM models include interactive isoprene emissions, which increase as climate warms, likely accounting for much of the difference relative to the other models. Leaving out the STOCHEM models, the correlations between water or ozone and CO drop to 0.28, and there is no clear relationship between the changes in OH and CO. It appears that in most of the models the oxidation of CO increases more than the oxidation of hydrocarbons, while the situation is reversed in the STOCHEM family. This difference highlights the impact of the variable treatment of hydrocarbon emissions and oxidation in the models' chemical schemes.

[50] Local changes were generally largest in the tropics, where they were of either sign (Figure 12). Some of these appear to be related to the persistent marine stratus cloud decks that form off the western coasts in the tropics. Changes in that region are especially apparent during October off of South America, where there is a shift in the vertical profile of CO with reductions near the surface and increases at upper levels. Similar behavior is seen near the surface off Africa and over the maritime continent, but not at upper levels, suggesting that decreased low-level precipitation may have lessened removal of soluble gases such as hydrogen peroxide, enhancing OH and thereby reducing CO. Changes in the cloud decks in these regions will have also influenced photolysis rates, again affecting chemistry. Note that climate models generally have difficulty simulating cloud and other physical properties in these areas, however. Over Brazil during October, near surface CO increases with relatively little change aloft, again perhaps indicative of locally increased precipitation and also reflecting the influence of increased tropical isoprene in the STOCHEM simulations.

[51] In the 350 hPa level, and to a lesser extent at 500 hPa, CO shows patterns of positive anomalies near the tropics flanked by negative anomalies to the north and south. GCMs generally show reduced overturning circulation as climate warms, with precipitation enhanced near the equator and reduced in the subtropics [Held and Soden, 2006]. The effects of such a change are complex, however, and may include both decreased upward transport from the polluted boundary layer and increased removal of soluble species within the ascending branch, and the opposite in the descending branch. This complexity makes identifying the fingerprints of circulation anomalies in a single chemical tracer quite difficult. Analysis of the underlying climate simulations can reveal more about the causes of the CO anomalies displayed here, but is beyond the scope of this intercomparison. Relative to the tropics, changes in the extratropics are comparatively homogeneous.

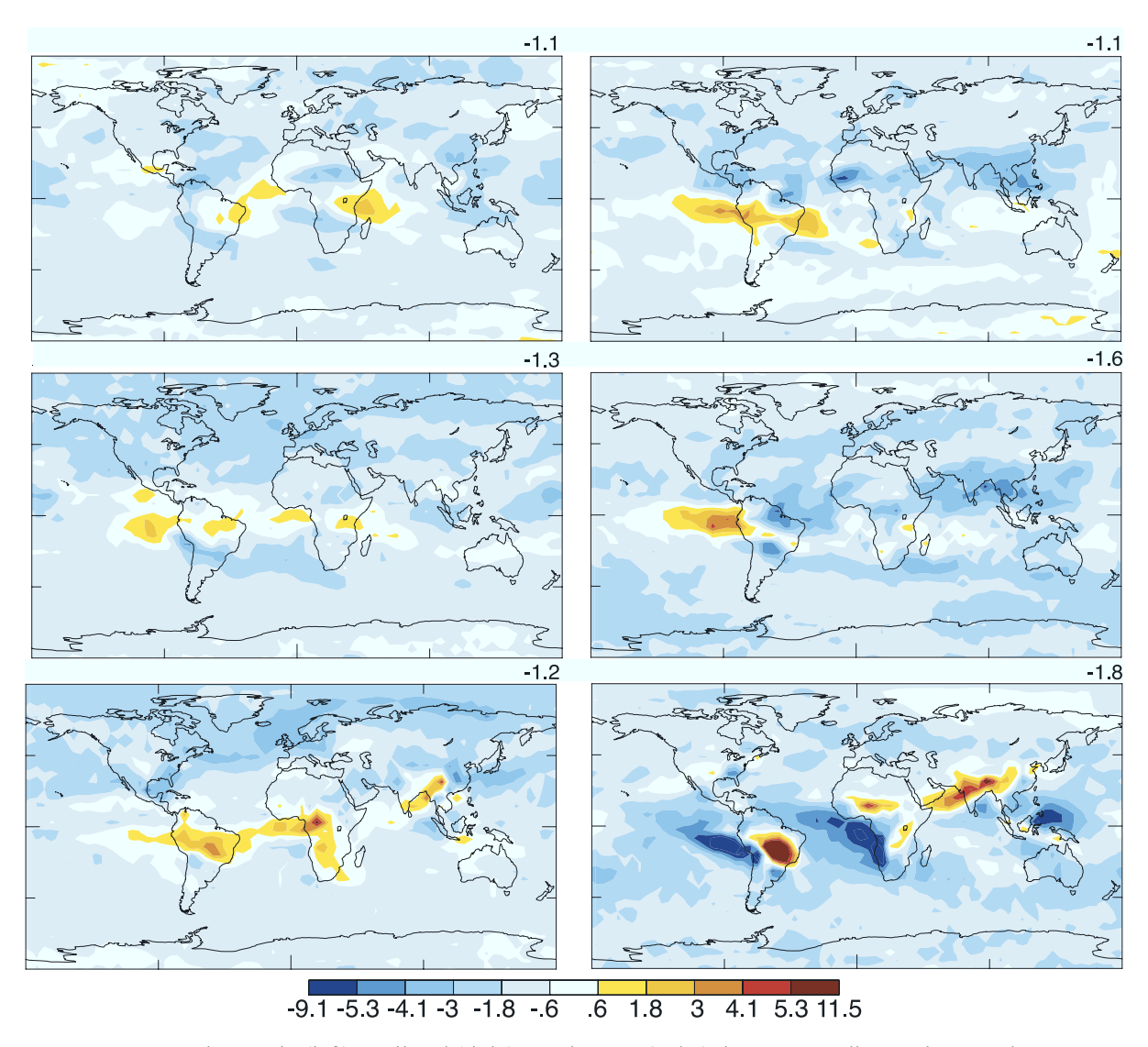


Figure 12. Changes in (left) April and (right) October CO (ppbv) due to 2030 climate change. The rows show descending vertical levels: (top) 300 hPa, (middle) 500 hPa and (bottom) 850 hPa.

[52] Interestingly, the projected multimodel mean decrease in CO resulting from climate change nearly offsets the increased CO from emissions in the CLE scenario, so that the global average change in CO with both projected emissions and climate changes (S5-S1) is near zero in all months. The tropics show the same near zero net changes. In the extratropics, however, while the changes are again near zero most of the year, there are weak increases in CO during boreal winter and early spring in the SH, and decreases at this time in the NH. The opposing behavior of the two hemispheres arises from the seasonality of the NH-dominated CO sink, as discussed previously.

6. Summary and Conclusions

[53] We have analyzed the simulations of carbon monoxide in a large ensemble of global chemical models. Compared with near-global satellite observations, the models are able to capture the broad spatial patterns of CO, with more pollution over and downwind of the industrialized parts of the NH and greater abundances near the surface. The

measured seasonality in the tropics and in the SH extratropics is also reproduced well. However, both the magnitude and seasonality of CO in the NH extratropics show large biases in the models in comparison with either satellite or surface data. We attribute these to a substantial underestimate of surface CO emissions, especially over east Asia, in the IIASA/ EDGAR3.2 inventory used by the models, a conclusion in line with recent inverse model studies [Arellano et al., 2004; Bergamaschi et al., 2000; Pétron et al., 2002, 2004] and a comparison of these same models with NO₂ observations [van Noije et al., 2006]. The comparison of CO with observations also demonstrated the difficulties associated with comparison of global models to point measurements, highlighting the value of near-global satellite data sets in model evaluation. The CO biases in the models would lead to an underestimate of ozone and an overestimate of OH in the NH extratropics, though these effects may not be large and could easily be overwhelmed by other factors.

[54] Though the model results were typically qualitatively similar, quantitative variations between the models' CO simulations were fairly large, attributable at least in large

Table A1. Overview of Models

References	Sudo et al. [2002a, 2002b, 2003]	Sudo et al. [2002a, 2002b, 2003]	Wild and Prather [2000], Wild et al. [2003]	Bey et al. [2001], Martin et al. [2003], Park et al.	Shindell et al. [2003, 2005b], Bell et al. [2005], Schmidt et al. [2006]	Rotman et al. [2001], Wild et al. [2003], Bev et al. [2001]	Rotman et al. [2001], Wild et al. [2003], Bey et al. [2001]	Rotman et al. [2001], Wild et al. [2003], Bey et al. [2001]	Müller and Brasseur [1995], Müller and Stavrakou [2005]	Rotman et al. [2004]	Sadourny and Laval [1984], Hauglustaine et al. [2004]	Sadourny and Laval [1984], Hanchystaine et al. [2004]	von Kuhlmann et al. [2003a, 2003b], Lawrence et al. [1999], Rasch et al. [1997]	von Kuhlmann et al. [2003a, 2003b], Lawrence et al. [1999], Rasch et al. [1997]	Brasseur et al. [1998], Hauglustaine et al. [1998], Horowitz et al. [2003]	Horowitz et al. [2003], The et al. [2005], Lamarque et al. [2005], L. K. Emmons et al. (manuscript in preparation, 2006)
Stratospheric Chemistry	O ₃ relaxed above 50 hPa to observations	O ₃ relaxed above 50 hPa to observations	LINOZ [McLinden et al., 2000]	SYNOZ: O ₃ production rate at 70 hPa: 500 Tg/yr [<i>McLinden et al.</i> , 2000]	O ₃ climatology based on satellite and sonde observations. NO _y set to prescribed NO _y O ₃ ratios	O ₃ influx from SYNOZ: 550 Tg/yr	O ₃ influx from SYNOZ: 550 Tg/yr	O ₃ influx from SYNOZ: 550 Tg/yr	zonal mean O ₃ prescribed above 98 hPa, zonal mean HNO ₃ prescribed above 50 hPa	full stratospheric chemistry, including Cl _x , Br _v	stratospheric O ₃ nudged toward climatology above 380 K	stratospheric O ₃ nudged toward climatology above 380 K	zonal mean O ₃ climatology above 30 hPa; above tropopause: NO _y set to prescribed NO _y /O ₃ ratios	zonal mean O ₃ climatology above 30 hPa; above tropopause: NO _y set to prescribed NO, O ₃ ratios	overwrite O ₃ above 14 hPa; between 14 hPa and tropopause relax to climatology (10 day time constant)	relaxed to <i>Logan</i> [1999] above tropopause; above 100 hPa
Tropospheric Chemistry	53 species, interactive SO ₄ aerosol	53 species, interactive SO ₄ aerosol	35 species (27 transported), using ASAD [Carver et al. 1997]	31 tracers (24 for O_x , 7 for SO_x -NH _x -NO _y aerosols, interactive)	35 species, 20 transported, interactive SO _x aerosol	85 species, off-line SO _x aerosol	85 species, off-line SO _x aerosol	85 species, off-line SO _x aerosol	60 species (40 transported), interactive SO _x aerosol	100 species, including C1 _x , Br _v	85 species	85 species	60 species	60 species	74 species, interactive SO _x , BC aerosols	96 species, aerosols SO _x , NH ₃ , NO ₃ , BC/OC, seasalt, SOA
Underlying Meteorology	CTM: ECMWF	GCM: CCSR/NIES	CTM: ECMWF-IFS pieced forecast data for 2000	CTM: GEOS winds, NASA GMAO	GCM:, ModelE GISS	GCM: NCAR MACCM3	CTM: GEOS-2-DAS assimilated fields for Mar 1997 to Feb 1998	GCM: GISS-2'	CTM: monthly means from ECMWF reanalyses (1993–2001 ERA40)	GCM: CAM3	CTM: nudged to ECMWF/ERA15-ERA40-OD	GCM: LMDz	CTM: ECMWF reanalysis	CTM: NCEP/NCAR reanalysis	CTM: NCEP reanalysis	GCM: CCSM3
Resolution (lon/lat/levels), Top Level	2.8°/2.8°/L32, 3 hPa	2.8°/2.8°/L32, 3 hPa	2.8°/2.8°/L37, 10 hPa	5°/4°/L30, 0.01 hPa	5°/4°/L23, 0.01 hPa	5°/4°/L52, 0.006 hPa	5°/4°/L46, 0.048 hPa	5°/4°/L23, 0.017 hPa	5°/5°/L25, 50 hPa	5°/4°/L26, 2 hPa	3.75°/2.5°/L19, 3hPa	3.75°/2.5°/L19, 3hPa	5.6°/5.6°/L28, 2 hPa	5.6°/5.6°/L28, 2 hPa	1.9°/1.9°/L28, 0.7 hPa	2.8°/2.8°/L26, 4 hPa
Contact Author	Kengo Sudo	Kengo Sudo	Oliver Wild	Isabelle Bey, Jerome Drevet	Nadine Unger, Drew T. Shindell	Jose M. Rodriguez, Susan Strahan	Jose M. Rodriguez, Susan Strahan	Jose M. Rodriguez, Susan Strahan	Jean-Francois Müller	Cynthia S. Atherton, Daniel J. Bergmann	Didier Hauglustaine, Sophie Szopa	Didier Hauglustaine, Sonhie Szona	Ξ	Tim Butler, Mark Lawrence	Arlene Fiore, Larry Horowitz	Jean Francois Lamarque
Model	CHASER_CTM	CHASER_GCM	FRSGC/UCI	GEOS-CHEM	GISS	GMI/CCM3	GMI/DAO	GMI/GISS	IASB	LLNL-IMPACT	LMDz/INCA-CTM	LMDz/INCA-GCM	MATCH-MPIC/ECMWF	MATCH-MPIC/NCEP	MOZ2-GFDL	MOZART4

[2003], MOZART-2 described by *Horowitz et al.* [2003] preparation, 2006), ECHAM5 described by Röckner et al. S. Rast et al. (manuscript in Zeng and Pyle [2003, 2005] Collins et al. [1997, 2003] Stevenson et al. [2004] Dentener et al. [2003], van Noije et al. [2004] Law et al. [1998, 2000] Dentener et al. [2003], Collins et al. [1997], Krol et al. [2005] Pitari et al. [2002] Sundet [1997] O₃ and NO_v prescribed above 30 hPa in tropics (10 day time constant) relaxed to stratospheric O₃, NO_x, and HNO₃ down to 200 hPa in scheme, including stratospheric O₃ fixed above 10 hPa based on climatology above tropopause above 123 hPa: except 30°N detailed stratospheric chemistry O₃ nudged toward climatology O₃ nudged toward climatology OsloCTM2 model run with prescribed O₃ concentration extratropics and 100 hPa relaxed toward SPARC O₃ (tropospheric chemistry operates below 30 hPa) Stratospheric O₃, HNO₃ and NO_x from stratospheric chemistry gradient at 100 hPa 30°S, above 60 hPa above 50 hPa 2D model aerosols 37 species (24 transported), 37 species (22 transported) 60 species (36 transported), 37 species (22 transported) SOx-NOy-NHx aerosols, SO_x-NOy-NHx aerosols. 70 species SO_x-NO_y-NH_x 70 species SO_x-NO_y-NH_x aerosols; interactive aerosols; interactive Includes tropospheric Tropospheric Chemistry 63 species SO₄ climatology no aerosols interactive no aerosol interactive aerosols 58 species CTM: ECMWF-IFS GCM: ULAQ-GCM 3-6-h operational 3-6-h operational Underlying Meteorology forecasts (2000) forecasts (2000) GCM: ECHAM5 GCM: HadGEM GCM: HadAM3 GCM: HadAM3 CTM: ECMWF CTM: ECMWF CTM: ECMWF analysis data forecast data operational vn4.5 vn4.5 0.48 hPa (1°/1° Europe, 100 hPa 3.75°/2.5°/L20, lon/lat/levels), 3.75°/2.5°/L19, 22.5°/10°/L26, N. America, 1.9°/1.9°/L31, Resolution 2.8°/2.8°/L40, 2.8°/2.8°/L31 Top Level 40 km 3°/2°/L25, 0.48 hPa and Asia) 6°/4°/L25, 0.04 hPa 10 hPa 4.6 hPa 10 hPa 10 hPa 5°/5°/L9, Veronica Montanaro, Michael Sanderson, Contact Author Martin G. Schultz, Kjerstin.Ellingsen, David Stevenson, Giovanni Pitari Michael Gauss Sebastian Rast Nick Savage, John A. Pyle Ruth Doherty wan van Noije Frank Dentener, Maarten Krol Bill Collins Guang Zeng, John Pyle STOCHEM-HadAM3 STOCHEM-HadGEM Model MOZECH and **MOZECH2** p-TOMCAT OsloCTM2 UM CAM ULAQTIM4 TM5

Table A1. (continued)

part to differences in the representation of NMVOC emissions and oxidation and in the models' removal of soluble gases in the hydrologic cycle. Factors such as differences in meteorology appear to be less important for large-area zonal means. The large differences between models were visible in all regions, including those for which the multimodel average agreed well with observations. Thus the good agreement seen in the tropics and SH extratropics is to some extent fortuitous. Better constraints on emissions of NMVOCs from observations could help increase understanding of whether individual models are biased because of model flaws or their emissions inventories. Given the variations in model representations of NMVOC emissions and oxidation, an intercomparison designed to remove these differences, perhaps by prescribing a "lowest common denominator" case (e.g., with few or even no NMVOCs) that all models could simulate identically, would greatly help to characterize the source of variations among models.

- [55] Projections of CO in 2030 are strongly influenced by the choice of emissions projection, with generally little global mean change in the CLE scenario, substantial decreases under MFR and large increases under A2. The CO response to 2030 conditions is inhomogeneous, with regional changes that depart significantly from the global behavior. These projected CO changes are quite robust across models, even at the regional level, and are largely driven by altered direct and indirect sources of CO, with only a small contribution from changes in the CO removal rate. The difference between the future scenarios highlights how the political and economic choices that determine the actual evolution of trace gas emissions will have a powerful and nearly immediate effect on short-lived pollutants such as CO.
- [56] The effects of projected 2030 climate changes are comparatively small. They roughly cancel the global mean increases in the CLE scenario, while in the other two scenarios their influence is minor relative to the large changes induced by emissions. Additionally, model results are less consistent even qualitatively with respect to the impact of climate change on the chemistry of CO, consistent with the results for ozone [Stevenson et al., 2006]. More work is clearly required to understand the interactions between climate change and atmospheric composition.

Appendix A

- [57] This appendix provides an overview of some of the key aspects of the participating models, including their resolution, meteorology, and a very brief summary of the chemical schemes (Table A1). References are provided in which more detailed information can be found.
- [58] Acknowledgments. D.T.S. and G.F. acknowledge the NASA Atmospheric Chemistry Modeling and Analysis Program. N.H.S., D.A.H., M.G.S., S.R. and S.Z. acknowledge EU FP5 project RETRO (EVK2-CT-2002-00170). N.H.S. also acknowledges NCAS for funding and supercomputing resources. M.G.S. and S.R. thank the DKRZ for computing resources and technical support. The multimodel study was coordinated through the ACCENT network of excellence.

References

Arellano, A. F. J., P. S. Kasibhatla, L. Giglio, G. R. van der Werf, and J. T. Randerson (2004), Top-down estimates of global CO sources using MOPITT measurements, Geophys. Res. Lett., 31, L01104, doi:10.1029/ 2003GL018609.

- Bell, N., D. Koch, and D. T. Shindell (2005), Impacts of chemistry-aerosol coupling on tropospheric ozone and sulfate simulations in a general circulation model, J. Geophys. Res., 110, D14305, doi:10.1029/ 2004JD005538.
- Bergamaschi, P., R. Hein, M. Heimann, and P. J. Crutzen (2000), Inverse modeling of the global CO cycle: 1. Inversion of CO mixing ratios, J. Geophys. Res., 105, 1909-1928.
- Bey, I., et al. (2001), Global modelling of tropospheric chemistry with assimilated meteorology: Model description and evaluation, J. Geophys. Res., 106, 23,073-23,095.
- Brasseur, G. P., D. A. Hauglustaine, S. Walters, P. J. Rasch, J.-F. Müller, C. Granier, and X. X. Tie (1998), MOZART, a global chemical transport model for ozone and related chemical tracers: 1. Model description, J. Geophys. Res., 103, 28,265-28,289.
- Carver, G. D., P. D. Brown, and O. Wild (1997), The ASAD atmospheric chemistry integration package and chemical reaction database, Comput. Phys. Commun., 105, 197-215.
- Collins, W. J., D. S. Stevenson, C. E. Johnson, and R. G. Derwent (1997), Tropospheric ozone in a global-scale three-dimensional Lagrangian model and its response to NOx emission controls, J. Atmos. Chem., 26, 223-274.
- Collins, W. J., R. G. Derwent, B. Garnier, C. E. Johnson, M. G. Sanderson, and D. S. Stevenson (2003), Effect of stratosphere-troposphere exchange on the future tropospheric ozone trend, J. Geophys. Res., 108(D12), 8528, doi:10.1029/2002JD002617.
- Deeter, M. N., et al. (2003), Operational carbon monoxide retrieval algorithm and selected results for the MOPITT instrument, J. Geophys. Res., 108(D14), 4399, doi:10.1029/2002JD003186.
- Deeter, M. N., L. K. Emmons, D. P. Edwards, J. C. Gille, and J. R. Drummond (2004), Vertical resolution and information content of CO profiles retrieved by MOPITT, Geophys. Res. Lett., 31, L15112, doi:10.1029/2004GL020235.
- Dentener, F., W. Peters, M. Krol, M. van Weele, P. Bergamaschi, and J. Lelieveld (2003), Interannual variability and trend of CH₄ lifetime as a measure for OH changes in the 1979-1993 time period, J. Geophys. Res., 108(D15), 4442, doi:10.1029/2002JD002916.
- Dentener, F., et al. (2005a), The global atmospheric environment for the next generation, Environ. Sci. Technol., 40, 3586-3594.
- Dentener, F. D., D. S. Stevenson, J. Cofala, R. Mechler, M. Amann, P. Bergamaschi, F. Raes, and R. G. Derwent (2005b), Tropospheric methane and ozone in the period 1990-2030: CTM calculations on the role of air pollutant and methane emissions controls, Atmos. Chem. Phys.,
- Dlugokencky, E. J., L. P. Steele, P. M. Lang, and K. A. Masarie (1994), The growth rate and distribution of atmospheric methane, J. Geophys. Res., 99, 17,021 – 17,043.
- Edwards, D. P., et al. (2004), Observations of carbon monoxide and aerosols from the Terra satellite: Northern Hemisphere variability, J. Geophys. Res., 109, D24202, doi:10.1029/2004JD004727.
- Emmons, L. K., et al. (2004), Validation of Measurements of Pollution in the Troposphere (MOPITT) CO retrievals with aircraft in situ profiles, J. Geophys. Res., 109, D03309, doi:10.1029/2003JD004101.
- Ferretti, D. F., et al. (2005), Unexpected changes to the global methane
- budget over the past 2000 years, *Science*, 309, 1714–1718. Gedney, N., P. M. Cox, and C. Huntingford (2004), Climate feedback from wetland methane emissions, Geophys. Res. Lett., 31, L20503, doi:10.1029/2004GL020919.
- Hauglustaine, D. A., G. P. Brasseur, S. Walters, P. J. Rasch, J.-F. Müller, L. K. Emmons, and M. A. Carroll (1998), MOZART, a global chemical transport model for ozone and related chemical tracers: 2. Model results and evaluation, J. Geophys. Res., 103, 28,291-28,335.
- Hauglustaine, D. A., F. Hourdin, S. Walters, L. Jourdain, M.-A. Filiberti, J.-F. Larmarque, and E. A. Holland (2004), Interactive chemistry in the Laboratoire de Météorologie Dynamique general circulation model: Description and background tropospheric chemistry evaluation, J. Geophys. Res., 109, D04314, doi:10.1029/2003JD003957
- Heald, C. L., et al. (2003), Asian outflow and trans-Pacific transport of carbon monoxide and ozone pollution: An integrated satellite, aircraft, and model perspective, J. Geophys. Res., 108(D24), 4804, doi:10.1029/ 2003JD003507
- Held, I. M., and B. J. Soden (2006), Robust responses of the hydrological cycle to global warming, J. Clim., in press.
- Horowitz, L. W., et al. (2003), A global simulation of tropospheric ozone and related tracers: Description and evaluation of MOZART, version 2, J. Geophys. Res., 108(D24), 4784, doi:10.1029/2002JD002853
- Kanakidou, M., et al. (1999), 3D global simulations of tropopsheric CO distributions: Results of the GIM/IGAC intercomparison 1997 excercise, Chemosphere Global Change Sci., 1, 263–282.
 Kasischke, E. S., E. J. Hyer, P. C. Novelli, L. P. Bruhwiler, N. H. F. French,
- A. I. Sukhinin, J. H. Hewson, and B. J. Stocks (2005), Influences of

- boreal fire emissions on Northern Hemisphere atmospheric carbon and carbon monoxide, *Global Biogeochem. Cycles*, *19*, GB1012, doi:10.1029/2004GB002300.
- Kiley, C. M., et al. (2003), An intercomparison and evaluation of aircraft-derived and simulated CO from seven chemical transport models during the TRACE-P experiment, J. Geophys. Res., 108(D21), 8819, doi:10.1029/2002JD003089.
- Krol, M., S. Houweling, B. Bregman, M. van den Broek, A. Segers, P. van Velthoven, W. Peters, F. Dentener, and B. Bergamaschi (2005), The two-way nested global chemistry-transport zoom model TM5: Algorithm and applications, *Atmos. Chem. Phys.*, 5, 417–432.
- Lamarque, J.-F., P. Hess, L. Emmons, L. Buja, W. Washington, and C. Granier (2005), Tropospheric ozone evolution between 1890 and 1990, *J. Geophys. Res.*, 110, D08304, doi:10.1029/2004JD005537.
- Law, K. S., P. H. Plantevin, D. E. Shallcross, H. L. Rogers, J. A. Pyle, C. Grouhel, V. Thouret, and A. Marenco (1998), Evaluation of modeled O₃ using Measurement of Ozone by Airbus In-Service Aircraft (MOZAIC) data, *J. Geophys. Res.*, 103, 25,721–25,737.
- Law, K. S., P. H. Plantevin, V. Thouret, A. Marenco, W. A. H. Asman, M. Lawrence, P. J. Crutzen, J. F. Müller, D. A. Hauglustaine, and M. Kanakidou (2000), Comparison between global chemistry transport model results and Measurement of Ozone by Airbus In-Service Aircraft (MOZAIC) data, J. Geophys. Res., 105, 1503–1525.
- Lawrence, M. G., P. J. Crutzen, P. J. Rasch, B. E. Eaton, and N. M. Mahowald (1999), A model for studies of tropospheric photochemistry: Description, global distributions, and evaluation, *J. Geophys. Res.*, 104, 26,245–26,277.
- Logan, J. A. (1999), An analysis of ozonesonde data for the troposphere: Recommendations for testing 3-D models and development of a gridded climatology for tropospheric ozone, *J. Geophys. Res.*, 104, 16,115–16,149.
- Martin, R. V., D. J. Jacob, R. M. Yantosca, M. Chin, and P. Ginoux (2003), Global and regional decreases in tropospheric oxidants from photochemical effects of aerosols, *J. Geophys. Res.*, 108(D3), 4097, doi:10.1029/2002JD002622.
- McLinden, C. A., S. C. Olsen, B. Hannegan, O. Wild, M. J. Prather, and J. Sundet (2000), Stratospheric ozone in 3-D models: A simple chemistry and the cross-tropopause flux, *J. Geophys. Res.*, 105, 14,653–14,666.
- Müller, J.-F., and G. P. Brasseur (1995), IMAGES: A three-dimensional chemical transport model of the global troposphere, *J. Geophys. Res.*, 100, 16,445–16,490.
- Müller, J.-F., and T. Stavrakou (2005), Inversion of CO and NOx emissions using the adjoint of the IMAGES model, *Atmos. Chem. Phys. Disc.*, 4, 7985–8068.
- Nakicenovic, N., et al. (2000), *IPCC Special Report on Emissions Scenarios*, 570 pp., Cambridge Univ. Press, New York.
- Novelli, P. C., K. A. Masarie, and P. M. Lang (1998), Distributions and recent changes of carbon monoxide in the lower troposphere, *J. Geophys. Res.*, 103(D15), 19,015–19,034.
- Olivier, J. G. J., and J. J. M. Berdowski (2001), Global emissions sources and sinks, in *The Climate System*, edited by J. Berdowski et al., pp. 33–78, A. A. Balkema, Brookfield, Vt.
- Palmer, P. I., D. J. Jacob, D. B. A. Jones, C. L. Heald, R. M. Yantosca, J. A. Logan, G. W. Sachse, and D. G. Streets (2003), Inverting for emissions of carbon monoxide from Asia using aircraft observations over the western Pacific, J. Geophys. Res., 108(D21), 8828, doi:10.1029/2003JD003397.
- Park, R. J., D. J. Jacob, B. D. Field, R. M. Yantosca, and M. Chin (2004), Natural and transboundary pollution influences on sulfate-nitrate-ammonium aerosols in the United States: Implications for policy, *J. Geophys. Res.*, 109, D15204, doi:10.1029/2003JD004473.
- Pétron, G., C. Granier, B. Khattatov, J.-F. Lamarque, V. Yudin, J.-F. Müller, and J. Gille (2002), Inverse modeling of carbon monoxide surface emissions using Climate Monitoring and Diagnostics Laboratory network observations, *J. Geophys. Res.*, 107(D24), 4761, doi:10.1029/2001JD001305.
- Pétron, G., C. Granier, B. Khattatov, V. Yudin, J.-F. Lamarque, L. Emmons, J. Gille, and D. P. Edwards (2004), Monthly CO surface sources inventory based on the 2000–2001 MOPITT satellite data, *Geophys. Res. Lett.*, 31, L21107, doi:10.1029/2004GL020560.
- Pitari, G., E. Mancini, V. Rizi, and D. T. Shindell (2002), Impact of future climate and emissions changes on stratospheric aerosols and ozone, J. Atmos. Sci., 59, 414–440.
- Prather, M. J., et al. (2001), Atmospheric chemistry and greenhouse gases, in *Climate Change 2001*, edited by J. T. Houghton, pp. 239–287, Cambridge Univ. Press, New York.
- Rasch, P. J., N. M. Mahowald, and B. E. Eaton (1997), Representations of transport, convection and the hydrologic cycle in chemical transport models: Implications for the modeling of short lived and soluble species, *J. Geophys. Res.*, 102, 28,127–28,138.

- Röckner, E., et al. (2003), The atmospheric general circulation model ECHAM 5. Part I: Model description, *MPI Rep. 349*, Max Planck Inst. for Meteorol., Hamburg, Germany.
- Rotman, D. A., et al. (2001), Global Modeling Initiative assessment model: Model description, integration, and testing of the transport shell, *J. Geo-phys. Res.*, 106, 1669–1691.
- Rotman, D. A., et al. (2004), IMPACT, the LLNL 3-D global atmospheric chemical transport model for the combined troposphere and stratosphere: Model description and analysis of ozone and other trace gases, *J. Geophys. Res.*, 109, D04303, doi:10.1029/2002JD003155.
- Sadourny, R., and K. Laval (1984), January and July performance of the LMD general circulation model, in *New Perspectives in Climate Modeling*, edited by A. Berger and C. Nicolis, pp. 173–197, Elsevier, New York.
- Schmidt, G. A., et al. (2006), Present day atmospheric simulations using GISS ModelE: Comparison to in-situ, satellite and reanalysis data, *J. Clim.*, 19, 153–192.
- Shindell, D. T., G. Faluvegi, and N. Bell (2003), Preindustrial-to-present-day radiative forcing by tropospheric ozone from improved simulations with the GISS chemistry-climate GCM, *Atmos. Chem. Phys.*, *3*, 1675–1702.
- Shindell, D. T., B. P. Walter, and G. Faluvegi (2004), Impacts of climate change on methane emissions from wetlands, *Geophys. Res. Lett.*, *31*, L21202, doi:10.1029/2004GL021009.
- Shindell, D. T., G. Faluvegi, and L. Emmons (2005a), Inferring carbon monoxide pollution changes from space-based observations, *J. Geophys. Res.*, 110, D23303, doi:10.1029/2005JD006132.
- Shindell, D. T., G. Faluvegi, N. Bell, and G. A. Schmidt (2005b), An emissions-based view of climate forcing by methane and tropospheric ozone, *Geophys. Res. Lett.*, 32, L04803, doi:10.1029/2004GL021900.
 Stevenson, D. S., R. M. Doherty, M. G. Sanderson, W. J. Collins, C. E.
- Stevenson, D. S., R. M. Doherty, M. G. Sanderson, W. J. Collins, C. E. Johnson, and R. G. Derwent (2004), Radiative forcing from aircraft NOx emissions: Mechanisms and seasonal dependence, *J. Geophys. Res.*, 109, D17307, doi:10.1029/2004JD004759.
- Stevenson, D. S., R. M. Doherty, M. G. Sanderson, C. E. Johnson, W. J. Collins, and R. G. Derwent (2005), Impacts of climate change and variability on tropospheric ozone and its precursors, *Faraday Disc.*, *130*, 41–57, doi:10.1039/b417412g.
- Stevenson, D. S., et al. (2006), Multi-model ensemble simulations of present-day and near-future tropospheric ozone, *J. Geophys. Res.*, 111, D08301, doi:10.1029/2005JD006338.
- Sudo, K., M. Takahashi, J. Kurokawa, and H. Akimoto (2002a), CHASER: A global chemical model of the troposphere: 1. Model description, J. Geophys. Res., 107(D17), 4339, doi:10.1029/2001JD001113.
- Sudo, K., M. Takahashi, and H. Akimoto (2002b), CHASER: A global chemical model of the troposphere: 2. Model results and evaluation, J. Geophys. Res., 107(D21), 4586, doi:10.1029/2001JD001114.
- Sudo, K., M. Takahashi, and H. Akimoto (2003), Future changes in stratosphere-troposphere exchange and their impacts on future tropospheric ozone simulations, *Geophys. Res. Lett.*, 30(24), 2256, doi:10.1029/ 2003GL018526.
- Sundet, J. K. (1997), Model studies with a 3-D global CTM using ECMWF data, Ph.D. thesis, Dep. of Geophys., Univ. of Oslo, Oslo, Norway.
- Tan, Q., W. L. Chameides, D. Streets, T. Wang, J. Xu, M. Bergin, and J. Woo (2004), An evaluation of TRACE-P emission inventories from China using a regional model and chemical measurements, *J. Geophys. Res.*, 109, D22305, doi:10.1029/2004JD005071.
- Tie, X., S. Madronich, S. Walters, D. P. Edwards, P. Ginoux, N. Mahowald, R. Zhang, C. Lou, and G. Brasseur (2005), Assessment of the global impact of aerosols on tropospheric oxidants, *J. Geophys. Res.*, 110, D03204, doi:10.1029/2004JD005359.
- van Aardenne, J., F. Dentener, J. Olivier, C. K. Goldewijk, and J. Lelieveld (2001), A $1^{\circ} \times 1^{\circ}$ resolution data set of historical anthropogenic trace gas emissions for the period 1890–1990, *Global Biogeochem. Cycles*, *15*, 909–928.
- Van der Werf, G. R., J. T. Randerson, G. J. Collatz, and L. Giglio (2003), Carbon emissions from fires in tropical and subtropical ecosystems, *Global Change Biol.*, 9, 547–562.
- van Noije, T. P. C., H. J. Eskes, M. van Weele, and P. F. J. van Velthoven (2004), Implications of the enhanced Brewer-Dobson circulation in European Centre for Medium-Range Weather Forecasts reanalysis ERA-40 for the stratosphere-troposphere exchange of ozone in global chemistry-transport models, *J. Geophys. Res.*, 109, D19308, doi:10.1029/2004JD004586.
- van Noije, T. P. C., et al. (2006), Multi-model ensemble simulations of tropospheric NO₂ compared with GOME retrievals for the year 2000, *Atmos. Chem. Phys.*, 6, 2943–2979.
- von Kuhlmann, R., M. G. Lawrence, P. J. Crutzen, and P. J. Rasch (2003a), A model for studies of tropospheric ozone and nonmethane hydrocarbons: Model description and ozone results, *J. Geophys. Res.*, 108(D9), 4294, doi:10.1029/2002JD002893.

- von Kuhlmann, R., M. G. Lawrence, P. J. Crutzen, and P. J. Rasch (2003b), A model for studies of tropospheric ozone and non-methane hydrocarbons: Model evaluation of ozone-related species, *J. Geophys. Res.*, 108(D23), 4729, doi:10.1029/2002JD003348.
- Wild, O., and M. J. Prather (2000), Excitation of the primary tropospheric chemical mode in a global 3-D model, *J. Geophys. Res.*, 105, 24,647–24.660.
- Wild, O., J. K. Sundet, M. J. Prather, I. S. A. Isaksen, H. Akimoto, E. V. Browell, and S. J. Oltmans (2003), CTM ozone simulations for spring 2001 over the western Pacific: Comparisons with TRACE-P lidar, ozonesondes and TOMS columns, *J. Geophys. Res.*, 108(D21), 8826, doi:10.1029/2002JD003283.
- Yurganov, L. N., et al. (2005), Increased Northern Hemispheric carbon monoxide burden in the troposphere in 2002 and 2003 detected from the ground and from space, *Atmos. Chem. Phys.*, 5, 563–573.
- Zeng, G., and J. A. Pyle (2003), Changes in tropospheric ozone between 2000 and 2100 modeled in a chemistry-climate model, *Geophys. Res. Lett.*, 30(7), 1392, doi:10.1029/2002GL016708.
- Zeng, G., and J. A. Pyle (2005), Influence of El Niño Southern Oscillation on stratosphere/troposphere exchange and the global tropospheric ozone budget, *Geophys. Res. Lett.*, 32, L01814, doi:10.1029/2004GL021353.
- M. Amann, International Institute for Applied Systems Analysis, A-2361 Laxenburg, Austria.
- C. S. Atherton and D. J. Bergmann, Atmospheric Science Division, Lawrence Livermore National Laboratory, Livermore, CA 94550, USA.
- I. Bey and J. Drevet, Ecole Polytechnique Fédéral de Lausanne, CH-1015 Lausanne, Switzerland.
- T. Butler, M. G. Lawrence, and M. G. Sanderson, Max Planck Institute for Chemistry, D-55128 Mainz, Germany.
- J. Cofala and S. Rast, Max Planck Institute for Meteorology, D-20146 Hamburg, Germany.
- W. J. Collins, Met Office, Exeter EX1 3PB, UK.
- F. J. Dentener, Institute for Environment and Sustainability, Joint Research Centre, European Commission, I-21020 Ispra, Italy.

- R. G. Derwent, rdscientific, Newbury RG14 6LH, UK.
- R. M. Doherty and D. S. Stevenson, School of Geosciences, University of Edinburgh, Edinburgh EH8 9YL, UK.
- K. Ellingsen, M. Gauss, and I. S. A. Isaksen, Department of Geosciences, University of Oslo, N-0317 Oslo, Norway.
- L. K. Emmons and J.-F. Lamarque, Atmospheric Chemistry Division, National Center for Atmospheric Research, Boulder, CO 80305, USA.
- H. J. Eskes and T. P. C. van Noije, Atmospheric Composition Research, Royal Netherlands Meteorological Institute, NL-3730 AE De Bilt, Netherlands.
- G. Faluvegi, D. T. Shindell, and N. Unger, NASA Goddard Institute for Space Studies, Columbia University, New York, NY 10025, USA. (dshindell@giss.nasa.gov)
- A. M. Fiore and L. W. Horowitz, Geophysical Fluid Dynamics Laboratory, NOAA, Princeton, NJ 08540, USA.
- D. A. Hauglustaine and S. Szopa, Laboratoire des Sciences du Climat et de l'Environnement, F-91191 Gif-sur-Yvette, France.
- M. C. Krol, Space Research Organisation Netherlands, NL-3584 CA Utrecht, Netherlands.
- V. Montanaro and G. Pitari, Dipartimento di Fisica, Università L'Aquila, I-67010 L'Aquila, Italy.
- J.-F. Müller, Belgian Institute for Space Aeronomy, B-1180 Brussels,
- G. Pétron, Global Monitoring Division, Earth System Research Laboratory, NOAA, Boulder, CO 80305, USA.
- M. J. Prather, Department of Earth System Science, University of California, Irvine, CA 92697, USA.
- J. A. Pyle, N. H. Savage, O. Wild, and G. Zeng, Centre for Atmospheric Science, University of Cambridge, Cambridge CB2 1EW, UK.
- J. M. Rodriguez and S. E. Strahan, Goddard Earth Science and Technology Center, Greenbelt, MD 21228, USA.
- M. G. Schultz, Institute for Chemistry and Dynamics of the Geosphere: Troposphere, Research Center Jülich, D-52425 Jülich, Germany.
- K. Sudo, Frontier Research Center for Global Change, Japan Agency for Marine-Earth Science and Technology, Yokohama 236-0001, Japan.